Department of Precision and Microsystems Engineering

Optimized Self-Centering Lens Mounting Technique for Precision Optomechanical Mounts in Supercontinuum Generation

Dan Hagemann

Report no : 2023.052
Coach : Andre Brouns
Professor : Nandini Bhattacharya
Specialisation : Opto-Mechanics
Type of report : Project Thesis
Date : August 7, 2023

Abstract

This work delves into the design and implementation of an optimized self-centering lens mounting technique for the collimator and coupler lenses in the Universal Light Source (ULS) by ASML, the leading supplier to the semiconductor industry. The ULS aims to meet the increasing demand for smaller logic nodes and higher throughput in optical metrology sensors. This light source employs a supercontinuum spectral shaping method based on a highly non-linear hollow core anti-resonance photonic crystal fiber filled with a high-pressure noble gas, necessitating highly stable and precise lens mounting.

This study thoroughly examines the existing lens mounting design, identifying its limitations in manufacturing, stability, and adhesive usage. To overcome these challenges, a self-centering design is proposed that leverages the geometrical relationship between thread angle, barrel and retaining ring diameters, and lens clearance to achieve precise alignment and minimize positioning errors. By optimizing these parameters, the centering error is substantially reduced, achieving a reduction in the order of tens of micrometers. This demonstrates a considerable improvement in centering precision compared to the current state-of-the-art method. Moreover, thermal effects are addressed through symmetrical design and local flexibility to reduce the effect of temperature fluctuations during operation and transportation, mitigating birefringences and tensile stresses.

An analytical assessment of five different collimator and coupler lens mount concepts is presented. The primary objective is to identify an optimal design that meets specific criteria related to operating temperature, stresses, eigenfrequency, and manufacturability. The study employs numerical analysis to evaluate the performance of each design concept relative to the currently employed mounting designs.

The resulting optimized self-centering coupler and collimator lens mount exhibits centering error, influenced by various tolerances. These tolerances have a deviation of $\pm 0.2\%$ for the lens radial surface, $\pm 1^{\circ}$ for the thread angle, and ± 0.2 mm for the remaining parameters. The calculated centering errors for coupler lens and collimator lens 1 and 2 are $6.27 \mu m$, $8.24\ \mu m$, and $6.98\ \mu m$, respectively. However, it is crucial to acknowledge that these results are purely theoretical and necessitate validation through experimental data to ascertain their accuracy. Consequently, further research is indispensable to confirm these values and ensure the reliability of the lens mount in practical applications.

Overall, this optimized self-centering technique offers enhanced stability, relaxed manufacturing tolerances, and eliminates the need for adhesives when compared to the current flexure design. These significant findings contribute to the advancement of optomechanical engineering and provide valuable insights into the implementation of self-centering mounts, thereby enhancing precision while relaxing manufacturing requirements in optomechanical mounting.

1 Introduction

The semiconductor industry is under constant pressure the achieve smaller logic nodes and higher throughput. This led ASML, the world's leading supplier for the semiconductor industry, to the exploration of a new light source for their optical metrology sensors. ASML is currently developing an Universal Light Source (ULS) that has high-quality broadband radiation, which can deliver a wide range of wavelengths and power outputs. The advantage of such a light source is that it can be implemented for most of their optical metrology sensors. The aim is to answer the increasing demand for more brightness, a wider application range, less noise, and lower operating costs.

The ULS is based on a supercontinuum spectral shaping method that uses the characteristics of a highly non-linear hollow core anti-resonance photonic crystal fiber (HCF). This fiber is made of transparent silica and the hollow core is filled with a high-pressure noble gas such as argon, xenon, or krypton. The fiber has microstructures around its fiber core, shown in Figure 1, that is optimized for a long propagation length with a small effective mode area and high chromatic dispersion properties.
The transmission of light is facilitated through the utilization of the anti-resonant Fabry-Pérot reflection principle. This principle dictates that when light travels through the fiber, it encounters the hollow capillaries surrounding the core, the reflected light from the first surface undergoes destructive interference with the light reflected from the second surface, resulting in minimal transmission losses [1]. Consequently, this mechanism is also referred to as thin-film interference, wherein the interference arises from the interaction of the reflected waves. An insightful investigation conducted by Chih-Hsien Lai et al. [2] expounded upon the guiding mechanism underlying such waveguides. In addition, solid core photonic crystal fibers with non-linear properties also offer the possibility of generating broadband radiation. However, UV radiation generated within the solid core may not appear in the fiber's output spectrum due to absorption by the solid material.

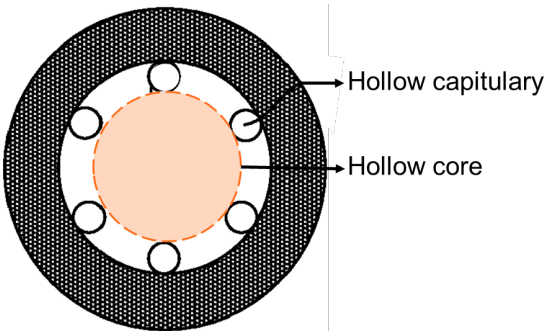

Figure 1: Structure of the HCF

The supercontinuum in the ULS is formed by directing a 50 Watt femtosecond 1030 nm wavelength (infrared) pulsed laser into the hollow core of the HCF shown in Figure 2. The electrons in the gas react non-linearly to the very strong electric field of the infrared pulses, broadening the spectrum of the light. This effectively results in a white light laser with a broad spectrum of similar intensity in the range of $350nm$ to $1200nm$. [3–10]. The HCF light source of this project and the method for manufacturing the HCF are patented in the European publication server [11].

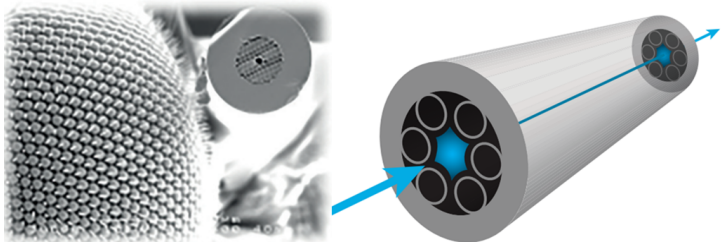

Figure 2: (Left) Image of the HCF and a fly's eye for scale. (Right) HCF in ISO-metric view [12]

The ULS consists of several essential components, namely an infrared laser, mirrors, coupling lenses for light focusing into the HCF, and collimator lenses responsible for collimating the outgoing light. Figure 3 provides a systematic view of the components in the ULS. This research project specifically concentrates on the mounting mechanism of the coupler and collimator lens assemblies, marked purple in Figure 3.

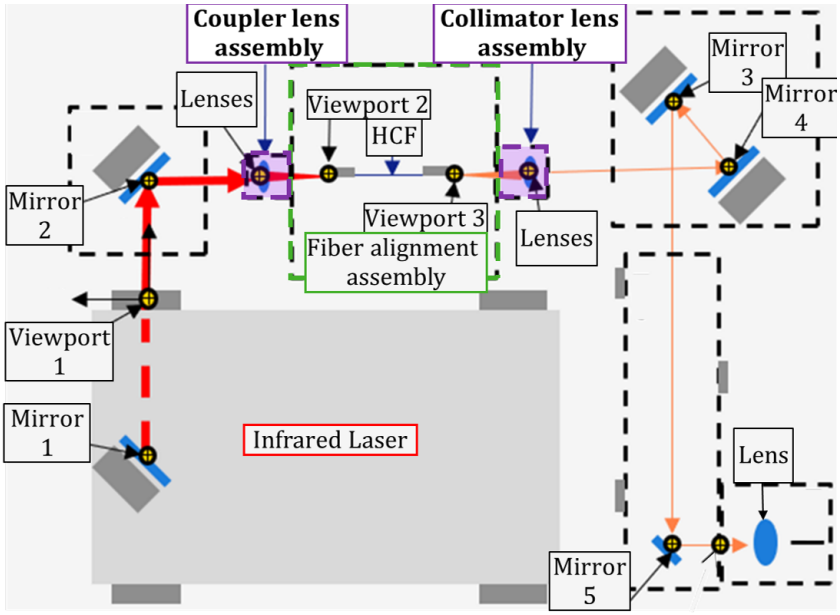

Figure 3: Components and subassemblies of the ULS. In purple the in-scope subassemblies

Upon closer examination of the component-level perspective depicted in Figure 4, we are presented with a schematic representation of the individual elements and their position relative to each other.

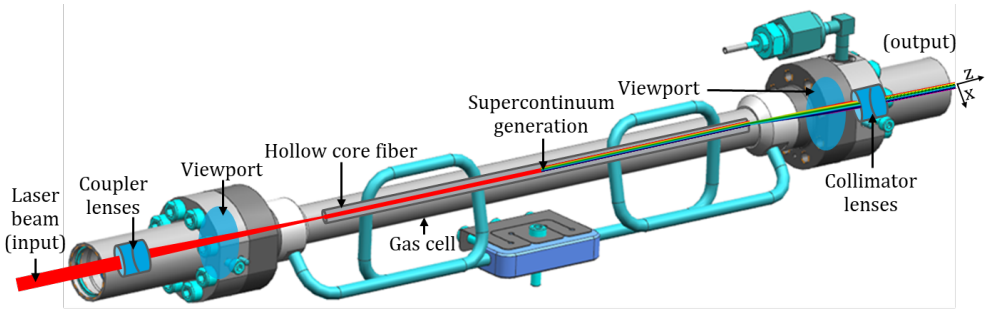

Figure 4: CAD model of Coupler lens, Collimator lens, and fiber alignment subassemblies with the optical components and light schematically depicted

The viewports located on both sides of the gas cell serve the dual purpose of confining the high-pressure noble gas and permitting the transmission of light.
The coupling lenses located at the input side of the fiber combine to make a cemented doublet, serving as a coupler between the laser beam with a diameter of 2.5 mm and the core of the HCF. The choice of a doublet lens is motivated by its property to be less prone to misalignment. Misalignment can arise due to deviations in the tip, tilt, or offset of the lens relative to the optical axis. Alignment adjustments can be made by slightly altering the positioning of the illumination spot on the lens, effectively modifying the optical path and aligning the system accordingly.
On the output side of the fiber, the collimator lenses combine to make an air-spaced doublet. Its primary function is to collimate the outgoing light, facilitating further propagation of the light. Given the susceptibility of the outgoing light to chromatic aberrations, the utilization of an air-spaced doublet lens becomes imperative. Notably, this doublet lens is not cemented together, as the supercontinuum encompasses UV light that will degrade the adhesive material.

1.1 Performance Requirements for Lens Mounting

The stability offered by the mount, in conjunction with the manufacturing tolerances, assembly tolerances, and measurement accuracy collectively contribute to the overall accuracy of the lens, as illustrated in Figure 5.

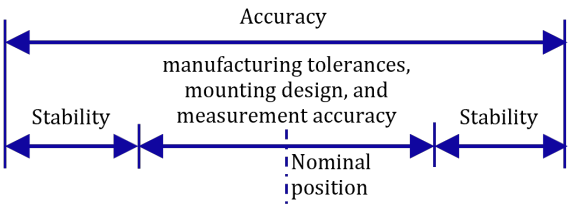

Figure 5: Accuracy and its components

An ideal optomechanical design has perfect accuracy, while simultaneously guaranteeing that the lens's position and orientation remain unaffected by the surrounding environment. In addition, the design must also account for temperature variations, dynamical vibrations, and mechanical stresses. Moreover, it places significant emphasis on preserving the geometry and alignment of

the optical elements to uphold the optical performance over its lifetime. This involves precise positioning and alignment of the lenses to optimize light transmission, minimize aberrations, and maximize the system's overall performance. However, achieving these conditions proves challenging in a practical design.

1.1.1 Vibrations

Vibrations occurring on the mount can induce resonances in the lens, leading to potential issues. These vibrations can be classified into two categories: periodic vibrations and random vibrations. The variables that play a crucial role in this context are the amplitude, frequency, and direction of the vibratory motion. To mitigate the resonances caused by vibrations, it is essential to incorporate strategically designed and strategically positioned damping mechanisms.
In the absence of any external driving force, the lens tends to undergo oscillations at a specific frequency known as the natural frequency or eigenfrequency. This behavior can be explained by considering the lens and mount as a mass-spring system, wherein the lens possesses a mass represented by m and the mount exhibits spring stiffness denoted by k. The natural frequency can be calculated using the equation:

$$\omega_0 = \sqrt{\frac{k}{m}}$$

When the vibration frequency closely or precisely matches the natural frequency of the lens, the amplitude of the vibration increases manyfold, thereby compromising the stability of the lens. To avoid this issue, it is crucial to design the lens mount in such a way that its natural frequency is safely higher than the anticipated driving forces. This can be achieved by increasing the stiffness of the mount, consequently elevating the natural frequency. The increase in natural frequency leads to a corresponding reduction in amplitude. The mount's stiffness is dependent upon two key factors: the geometric design and the specific stiffness of the material. The specific stiffness refers to the elastic modulus per mass density of the material. High stiffness is necessary for the mount to effectively remain stable and resist deformations caused by manufacturing processes, gravitational forces, and operational vibrations [13–15].

1.1.2 Coupling Efficiency

The primary objective driving the design of the ULS lies in maximizing the stability of the light source's output power. The coupling efficiency, characterized by its Gaussian distribution profile, serves as a fundamental factor in determining the overall performance of the system. The blue region highlighted in Figure 6 represents a coupling efficiency of 95% or higher that meet the stability requirement of the ULS. Within this region, the effects of vibrational disturbances on the coupling losses are mitigated to a considerable extent, as compared to the region situated beyond the 95% threshold. Therefore, maintaining a coupling efficiency within this critical range serves as a key criterion for guaranteeing the stability and reliable performance of the ULS system.

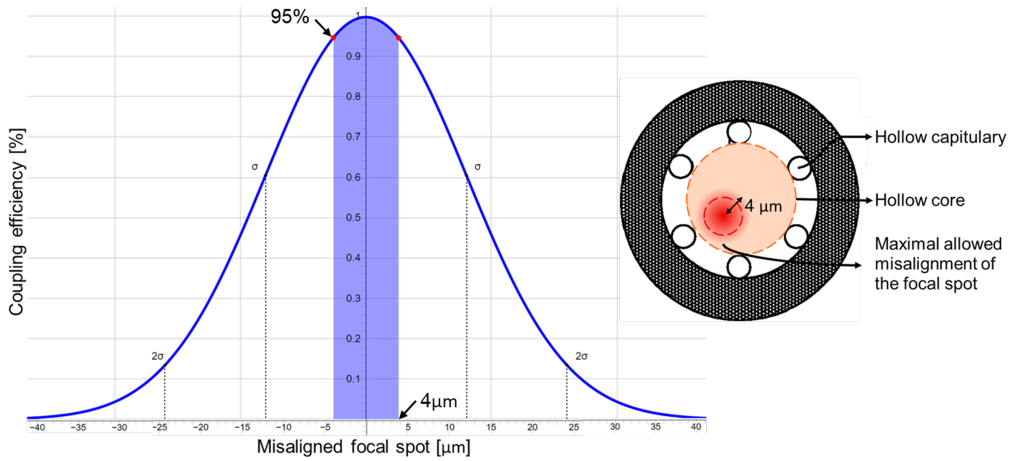

Figure 6: (Left): Representation of the coupling efficiency as a function of a lateral misalignment error of the focal spot. (Right): Visualisation of maximal allowed misalignment

The coupling characteristics of the HCF can be more accurately described as mode-coupling due to its non-linear properties, where the loss of mode leads to coupling losses. From a geometrical optics perspective, efficient coupling of a laser beam into the fiber occurs when the beam's divergence angle is smaller than the numerical aperture (NA) of the fiber core. In this case, an infrared laser with a 14 μm spot size and a Gaussian intensity distribution is directed on the sub-50 μm fiber core. It can be stated that the coupling efficiency is influenced by the spot location, spot stability, and beam quality.

Several factors affect the spot location and beam quality, with alignment errors being the primary contributors. These alignment errors encompass lateral error, longitudinal error, and angular error. A longitudinal error causes an increase in spot size and alters the energy distribution at the incident face of the fiber. A larger spot size requires greater control over lateral and angular alignment to achieve efficient coupling. Furthermore, a significant longitudinal error can lead to the spot size exceeding the diameter of the fiber core, resulting in reduced coupling efficiency.

The angular error primarily affects coupling efficiency by causing the incidence angle to exceed the NA of the fiber, leading to leakage of the beam out of the fiber core. A study conducted by Xingyang Liu et al. [16] emphasizes the substantial influence of lateral error on the power distribution of the Gaussian beam, relative to longitudinal error and angular error. Alignment errors, such as thermal drift, design geometry, and manufacturing tolerances, are likely sources of these discrepancies.

The system can be calibrated by adjusting the incident beam to align with the center of the coupling lens, thereby compensating for lateral and angular alignment errors. This mitigates the position tolerance to allow for a maximal offset of $\pm 50 \mu m$.

Coupling losses can also occur due to spot instability, wherein the spot partially vibrates outside the fiber core. To maintain coupling efficiency above 95%, spot stability must be within tight constraints of subμm and subμrad [17].

1.1.3 Polarization

Supercontinuum generation, a phenomenon influenced by the polarization state of the incident laser, exhibits a direct impact on conversion efficiency. Specifically, the resulting supercontinuum retains the same polarization state as the incident laser. In a study conducted by Antoine Proulx et al. [18], it was found that linear polarization is the preferred configuration for supercontinuum generation. However, it is crucial to address polarization loss, which occurs when the lens undergoes deformation, leading to the development of internal stresses. These stresses induce anisotropic and inhomogeneous behavior, resulting in birefringence. Consequently, birefringence affects the refraction of light rays within the lens and alters their polarization state. As a consequence, uneven spectral broadening and distortion may occur in the generated supercontinuum spectrum, compromising its quality and coherence. Additionally, polarization fluctuations can undermine the stability of polarization and impede polarization-dependent applications of the supercontinuum source. It is important to note that any energy present in alternative polarization states can be regarded as inefficiently contributing to the generation of a supercontinuum, thereby diminishing the overall conversion efficiency [19, 20].

1.1.4 Thermal Expansion

Thermal expansion is a fundamental property of matter, referring to its tendency to change in shape, area, volume, and density in response to temperature fluctuations. When a substance is heated, its constituent molecules exhibit heightened vibrational and translational motion, resulting in increased intermolecular spacing. The ratio of the relative expansion to the change in temperature is referred to as the material's coefficient of linear thermal expansion (CTE), which generally exhibits variability with temperature. The effects of thermal expansion, contraction, and cycling can introduce mechanical stress and loosening of the lenses which may lead to misalignment.

In a well-constrained system, it is possible to define a specific point within the system that remains unaffected by temperature changes, known as the thermal center. To achieve this, it is essential that the system is not over-constrained and permits uniform thermal expansion. By aligning the thermal center with the center of the lens, it becomes possible to attain a high level of thermal stability [21–25]. In Figure 7, three examples are depicted to illustrate systems that have the thermal center in the center of the optical element for high thermal stability.

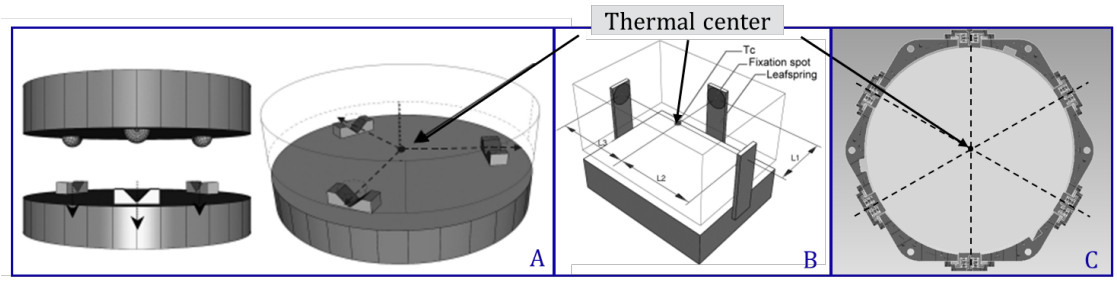

Figure 7: A: Kinematic mount with 3 balls and V-grooves. B: Mount with 3 leaf springs [21]. C: Radial spring support [25]

During operation, the lenses are subjected to irregular thermal loads resulting from the light that

is absorbed. This results in temperature changes which introduce differential thermal expansion and contraction between the lens and mount. It is worth noting that the mount material typically possesses a higher CTE compared to the lens material. Therefore, a decrease in temperature causes the mount to contract to a greater extent than the lens. Consequently, this creates a compressive force acting upon the lens, resulting in the introduction of stress. These stresses can lead to reduced conversion efficiency or even failure of the lens. Additionally, they may induce plastic deformation of the mount. Conversely, an increase in temperature causes the mount to expand away from the lens. This expansion diminishes the clamping forces and, unless the lens is securely glued in place, it potentially allows the lens to shift under external forces [26].

The practical application of this theory was demonstrated in a study conducted by Stephen Smee, who designed a novel flexure mount capable of accommodating large temperature excursions. The successful design, depicted in Figure 8 A, was utilized for mounting lenses ranging from 25 mm to 375 mm, operating within a temperature range spanning from ambient temperature to 77 K [27]. In addition, a study conducted by T. Froud et al. [28] presented a case of design failure resulting from a CTE mismatch, as shown on the left in Figure 8 B. However, through the introduction of low thermal expansion pads with optimized adhesion type and thickness the stresses were reduced to acceptable levels, addressing the issue as illustrated on the right in Figure 8 B.

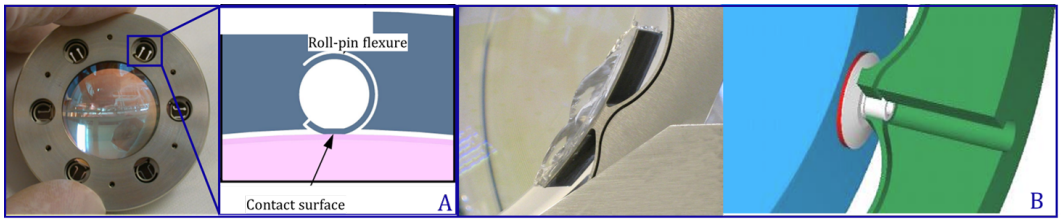

Figure 8: A: Novel roll-pin flexure [27]. B: Lens failure (left), successful re-design (right) [28]

The lens mounts face even more substantial temperature fluctuations during handling and transport, in addition to the thermal loads experienced during operation. These fluctuations can range from -25°C to 60°C, and it is of utmost importance for the lens assembly to withstand this without cracks, breakage, or diminished performance.

1.1.5 Adhesive Bonding

Adhesive bonding is a widely employed assembly technique that involves joining two surfaces using an adhesive substance. This method offers several advantages, including improved distribution of contact stress and the ability to dampen shock and vibration. However, it also introduces certain considerations that must be carefully addressed to ensure optimal performance. These considerations encompass bond strength, coefficients of thermal expansion, out-gassing, lifetime, cure shrinkage, and ultraviolet (UV) resistance. Additionally, factors such as the area and thickness of the adhesive layer, as well as the cleanliness of the bond surfaces, play crucial roles in the design process.

Optical adhesives can be classified into three main categories: epoxy resins, flexible adhesives, and UV-curable adhesives. Epoxy resins typically necessitate a relatively larger layer thickness, thereby rendering the process of index matching more critical. Conversely, UV-curable adhesives offer faster curing times and exhibit lower levels of shrinkage and out-gassing when compared to epoxy adhesives. Mechanical properties, such as tensile and peel strengths, tend to be similar

among these different types of adhesives. However, it is important to note that the specific properties and performance characteristics of adhesives can vary significantly depending on their formulation, composition, and curing conditions. Consequently, a thorough understanding of the intended application and the corresponding requirements is vital for selecting the most suitable adhesive for a given scenario. Moreover, extensive testing and analysis should be conducted to evaluate the performance and durability of the adhesive bond in order to ensure its long-term reliability and effectiveness. Furthermore, it is important to acknowledge that all adhesives possess inherent vulnerability to UV light. Recent tests have revealed a concerning issue wherein the backscattered UV light originating from the light source is detected in the coupler lens. This finding indicates that adhesive bonding can pose a significant risk to the lifetime of both the coupler and collimator mounts [29–34].

1.1.6 Clamping

Clamping, a commonly employed technique for attaching optical lenses to metal, involves the utilization of mechanical clamps or retaining rings to secure the lenses within a metal frame or mount. The effectiveness of this fastening method relies on the friction coefficient and the application of a clamping force to achieve the desired level of friction. This frictional force ensures a secure connection between the lens and the metal frame. It is crucial to exercise caution during the tightening process to avoid overtightening the clamps, as excessive pressure can lead to detrimental consequences such as lens cracking or breakage. To achieve an optimal pressure level, it is imperative to employ a force-controlled tool during the tightening process. One such tool that ensures tightening pressure is a torque wrench.

The pressure is a result of the elastic deformation of the material and design features, resulting in the introduction of contact stress. Contact stress is the combined effect of compressive stress within the contact boundary and tensile stress just outside the contact boundary, as depicted in Figure 9. It is important to note that glass-like materials, such as the coupler and collimator lenses, are significantly weaker to tensile stress as opposed to compressive stress. glass-like materials, by their nature, are characterized by a limited ability to deform plastically and are prone to fracture or failure under tensile loads.

To evaluate these contact stresses accurately, the preferred method is to employ Hertzian contact stress calculations. Wenrui Cai et al. conducted a comprehensive study in which they applied this method to analyze the strengths of glass materials [35].

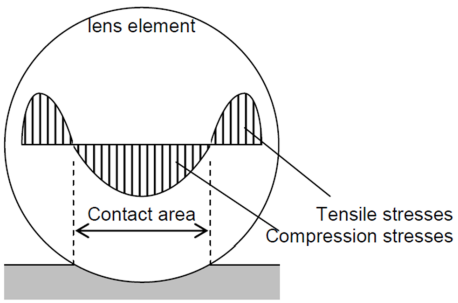

Figure 9: Hertzian contact between a lens element and a flat clamping surface, including stress schematics [36]

It is worth mentioning that the contact area, determined by the shape of the contact region, plays a significant role in influencing the magnitude of the contact stresses. The contact shape can vary from a sharp contact, offering the highest level of accuracy but also generating the highest contact stress, to a conformal contact, which results in lower stress levels [37]. This shape variation is demonstrated in Figure 10.

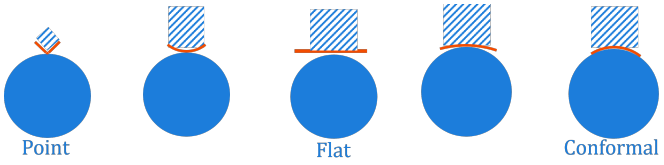

Figure 10: Illustration of different contact shapes

A comprehensive list of commonly employed optical mounting designs can be found in the references [38–41]. Illustrative instances of such mounting mechanisms are presented in Figure 11.

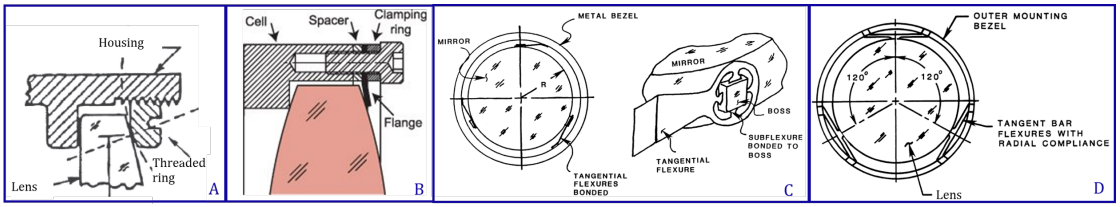

Figure 11: A: Barrel design with a threaded ring [38]. B: Barrel design with a flange [39]. C: Flexure design with subflexures. D: Radial complained flexures [40]

Among these designs, particular attention is drawn to mounting mechanisms incorporating flexures, primarily owing to their inherent capacity to achieve exceptional levels of accuracy. Studies have consistently demonstrated that flexure mounts are widely regarded as the preferred method for achieving high accuracy in optical mounting. The preference for flexure mounts stems from the inherent disadvantage of rigid mounts, namely their propensity to generate higher levels of contact stresses compared to flexure mounts. These elevated contact stresses will potentially impair the optical performance of the lens [42–45]. Although flexure mounts can be implemented without the need for adhesive bonding, it is worth noting that in many instances, flexure mounts are used in conjunction with adhesives. Adhesive bonding introduces several challenges, as discussed in the previous chapter.

The mounting of multiple lenses often employs the widely used assembly method of inserting them into a metal barrel. This barrel design offers several advantages, such as high stiffness, short assembly time, reduced stain on manufacturing and assembly tolerances, and the ability to replace the lenses. However, a notable drawback is the compromise in centering precision. In situations where greater precision is required, a barrel design may not be suitable. Nonetheless, a study conducted by Frédéric Lamontagne et al. in 2015 presented an innovative approach to address this limitation. The researchers accomplished this by optimizing the geometric parameters of the barrel design to enable the self-centering of the lens. According to their findings, lens centering with an accuracy below 6.5 μm is attainable by utilizing threaded rings [46]. This advancement

contributes significantly to the field of optomechanical lens mounting and opens up possibilities for further improvements.

1.1.7 Lens Self-Centering in a Barrel Designs

Typical barrel designs serve as the default choice for connecting optical components in a wide range of instruments, including cameras, binoculars, small telescopes, and modular components utilized in optical laboratory prototyping. A typical lens barrel design involves placing a lens into a barrel and securing it in place using a threaded ring. Threaded rings require clearance in the threads for assembly, leaving room for potential decentering or tilting.

Despite manufacturing precision advancements, the lenses and the mechanical mounts inevitably possess dimensional and geometric errors. Additionally, manufacturing tolerances associated with assembled components, such as thread radial clearance, lens surface quality, and variation in lens thickness, also contribute to the overall centering quality. Consequently, the performance of the theoretically perfect optical system may be diminished. Attaining the necessary level of precision for accurate lens positioning places a significant burden on the manufacturing processes involved in producing both the lens and the barrel.

The typical barrel design may reduce the centering errors by utilizing tight tolerances on threaded clearance, lens, and barrel diameter. By minimizing the radial clearance between the lens and the barrel inside diameter, centering errors typically ranging between 25 μm and 50 μm can be achieved [47, 48].

The level of precision achieved in lens centering within a typical barrel design is primarily determined by the radial thread clearance necessary for the threaded connection. This clearance enables the retaining ring to move off-center, leading to a contact point rather than a contact line, as illustrated in Figure 12. It is important to note that this contact point only constrains one degree of freedom (DoF), thereby permitting lens movement in the remaining five DoFs.

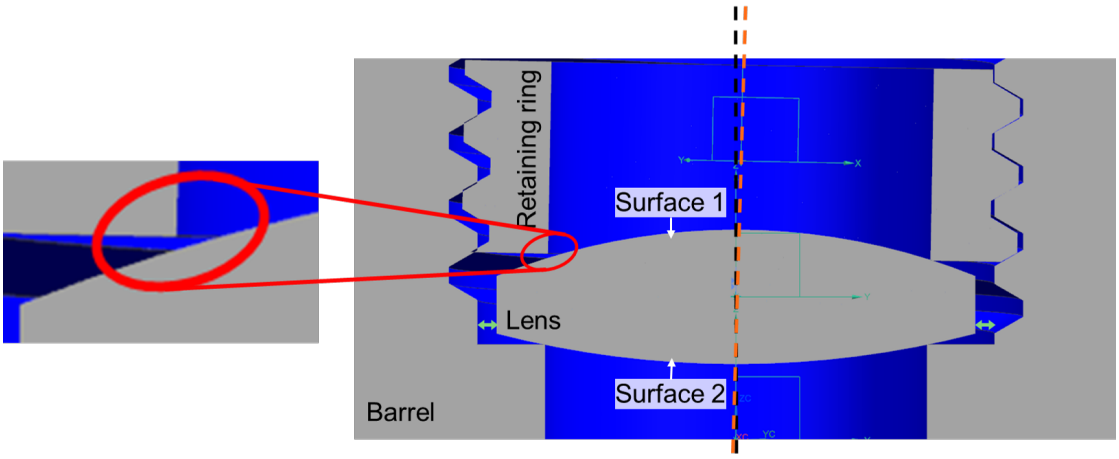

Figure 12: Decentered retaining ring leads to a gap and contact point between a centered lens and retaining ring. The barrel axis and retaining ring axis are depicted in black and orange respectively

To accurately define the lens centering error in relation to the barrel reference axis, it is essential

to consider both lens surfaces. When the retaining ring is tightened, it exerts a clamping force that displaces the lens off-center in order to completely constrain it, as visually depicted in Figure 13. The specific shape of the lens's second surface, whether convex, concave, positive meniscus, negative meniscus, plano-convex, or plano-concave, determines the behavior of the centering error. When the lens's second surface is either convex, concave, positive meniscus, or negative meniscus, the tightening of the retaining ring results in a rotational movement of the lens around the radial center of surface 2. This rotational displacement causes a centering error to occur. Conversely, when dealing with a plano-convex or plano-concave lens, the centering error manifests as a horizontal shift rather than a rotational movement.

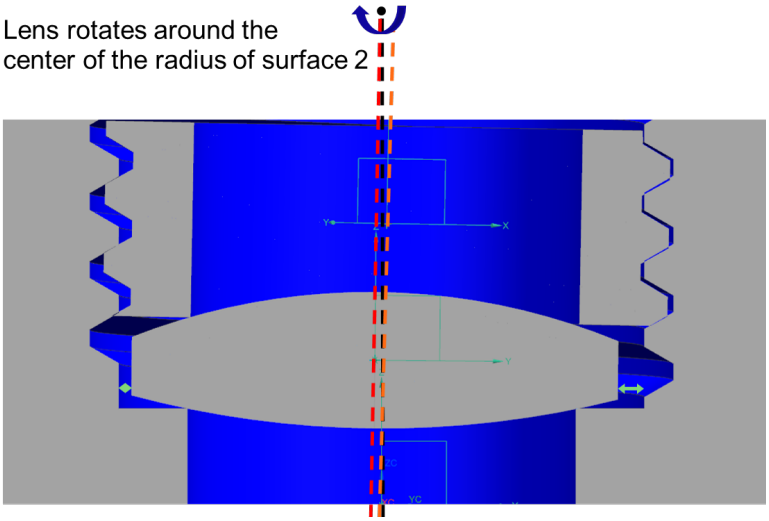

Figure 13: The lens rotates around the center of the radius of surface 2 till fully constrained by the retaining ring

In response to these centering errors, the concept of self-centering lenses has emerged with the main objectives to reduce positioning errors and relaxing manufacturing tolerances. This novel auto-centering lens mounting method by Frédéric Lamontagne et al. [46, 49–52] offers a solution to improve upon the limitations of the barrel design. This approach leverages the geometrical relationship between the lens diameter, lens radius of curvature, and the thread angle. By selecting an appropriate thread angle to correspond with the lens surface accordingly, auto-centering conditions can be achieved. In these conditions, any decentering or tilt of the retaining ring has counterbalancing effects on the centering of the lens.

To achieve these self-centering conditions, let us examine the relationship between the retaining ring and the lens surface it contacts. The tilt of the retaining ring is determined by the curvature of the lens surface that comes into contact with it. We can calculate the lateral decentering of the center of curvature of this lens surface resulting from the tilted retaining ring using Equation 1 [46]. The parameters used in this equation are depicted in Figure 14.

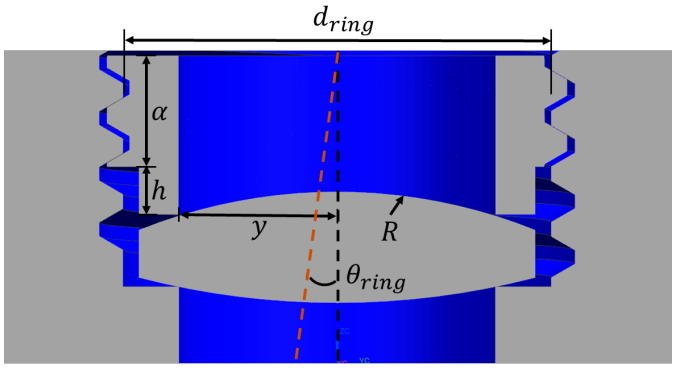

Figure 14: Parameters $\alpha,\ h,\ y,\ R,\ and\ \theta_{ring}$

$$\Delta_{tilt} = \left(\sqrt{R^2 - y^2} + h + \alpha/2\right) sin(\theta_{ring}) \tag{1}$$

The parameter:

- Δ_{tilt} [mm] represents the lateral decentering of the center of curvature of the lens surface in contact with the retaining ring resulting from the tilted retaining ring
- R [mm] represents the radius of the lens surface 1.
- y [mm] represents the radius of the contact circle.
- θ_{ring} [degrees] represents the tilt angle of the retaining ring relative to the barrel reference axis.
- h [mm] represents the distance between the thread and lens.
- α [mm] represents the thread depth.

The radial clearance between the barrel and retaining ring makes a tilt of the retaining ring possible. When the retaining ring shifts to the right, it is allowed to tilt because of the slope in the thread, as shown in Figure 15.

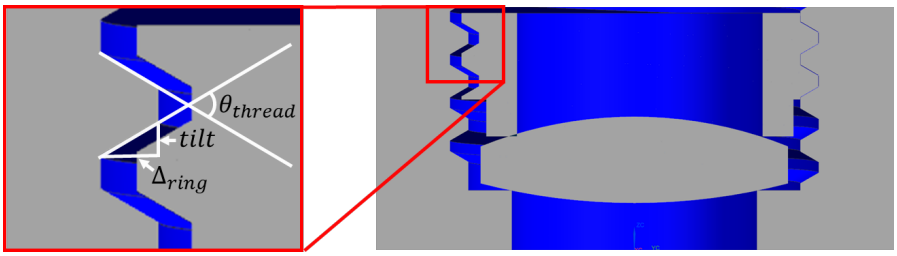

Figure 15: Parameters $\theta_{thread},\ tilt,\ \Delta_{ring}$

The parameter:

- θ_{thread} represents the thread angle. This is on an ISO metric thread always 60 degrees.
- $tilt$ represents the vertical tilt.

- Δ_{ring} represents the lateral decenter of the retaining ring.

The lateral decenter of the retaining ring, denoted as Δ_{ring}, is directly proportional to the lateral clearance in the thread connection. In other words, Δ_{ring} represents the amount of lateral displacement of the retaining ring caused by the clearance in the thread connection.

The movement of the retaining ring is influenced by the angle and size of the threads. This distance can be characterized from both the perspective of the thread and the perspective of the retaining ring. Interestingly, the equations for vertical tilt from these two viewpoints are equal to each other, as expressed in Equation 2.

$$\frac{1}{2}d_{ring}sin(\theta_{ring}) = \Delta_{ring}tan\left(\frac{\varphi_{threads}}{2}\right) = vertical\ tilt \tag{2}$$

To establish an expression for the tilt angle that is not dependent on the vertical tilt itself, we can rewrite the equation as shown in Equation 3 [46]. This equation establishes the correlation between the decentering of the threaded ring and the tilt of the retaining ring. When the retaining ring is shifted to the left, it undergoes a counterclockwise tilt. Conversely, when the retaining ring is moved to the right, it experiences a clockwise tilt. This is visually demonstrated with a plano-convex lens in Figure 16.

$$\theta_{ring} = sin^{-1}\left(\frac{2\Delta_{ring}tan\left(\frac{\varphi_{thread}}{2}\right)}{d_{ring}}\right) \tag{3}$$

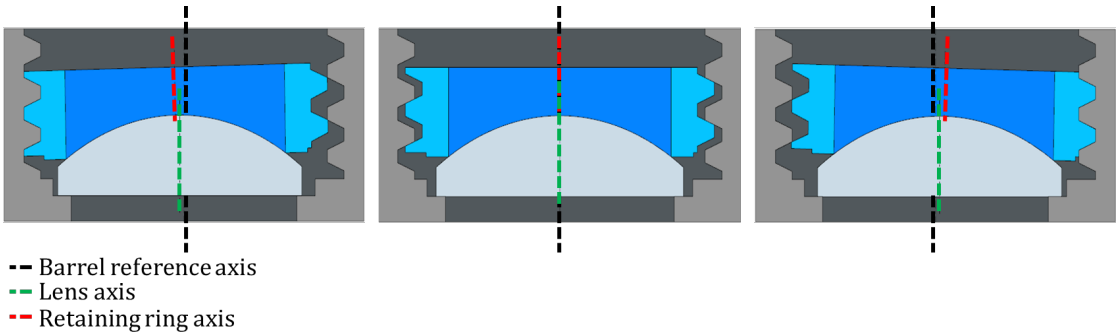

Figure 16: The tilted retaining ring introduces a centering error in the lens relative to the barrel reference axis

Consequently, we can substitute the expression for the tilt angle θ_{ring} into the equation for the lateral decentering of the center of curvature of the lens surface in contact with the retaining ring Δ_{tilt}. This yields the expression shown in Equation 4, which can be used to calculate the decentering of the lens as a function of the mount's parameters [46].

$$\Delta_{tilt} = \left(\sqrt{R^2 - y^2} + h + \frac{\alpha}{2}\right)\frac{2\Delta_{ring}tan\left(\frac{\varphi_{thread}}{2}\right)}{d_{ring}} \tag{4}$$

The decentering of the retaining ring is typically the maximum radial clearance present in the thread when it is screwed into the barrel.

The ISO (International Organization for Standardization) metric screw thread is universally acknowledged as the international standard and is defined in the ISO 68 publication. In the case

of an ISO metric screw thread, the thread clearance Δ_{ring} can be determined by Equation 5 which is dependent on the thread angle and the thread pitch P.

$$\frac{P}{4\tan\left(\frac{\varphi_{thread}}{2}\right)} \tag{5}$$

The tolerances are also specified in the ISO 68 and categorized into classes, namely classes 4, 5, 6, 7, and 8 for minor diameter tolerance of nut thread, and 4, 6, and 8 for major diameter tolerance of bolt thread. The tolerances are linked to the pitch and class specifications and can vary in magnitude, spanning a range of 36 μm to 1.25 mm. Detailed information can be found in Tables 7 and 8 of the ISO 68 publication [53].

To achieve lens centering, it is crucial to minimize or eliminate the decentering of the center of curvature of the lens surface in contact with the retaining ring in relation to the barrel reference axis. As previously discussed, this decentering is equivalent to the centering error resulting from the retaining ring's displacement caused by the clearance in the thread connection. Consequently, the self-centering condition can be established by upholding Equation 6, which captures the necessary criteria for achieving a self-centering mounting [46].

$$\Delta_{tilt} = \Delta_{ring} \tag{6}$$

Once the self-centering condition described in Equation 6 is met, it becomes possible to rephrase Equation 4 to Equation 7 in order to determine the exact angle at which the threads should be positioned to achieve self-centering. This adjustment ensures that the rotational center of the retaining ring aligns precisely with the center of the lens surface 1.

$$\varphi_{thread} = 2tan^{-1}\left(\frac{d_{ring}}{2\sqrt{R^2 - y^2} + 2h + \alpha}\right) \tag{7}$$

It is crucial to emphasize that the self-centering condition remains unaffected by the tilt of the retaining ring in relation to the barrel reference axis. The tilt of the retaining ring corresponds to the radius of curvature of lens surface 1, as illustrated in Figure 17.

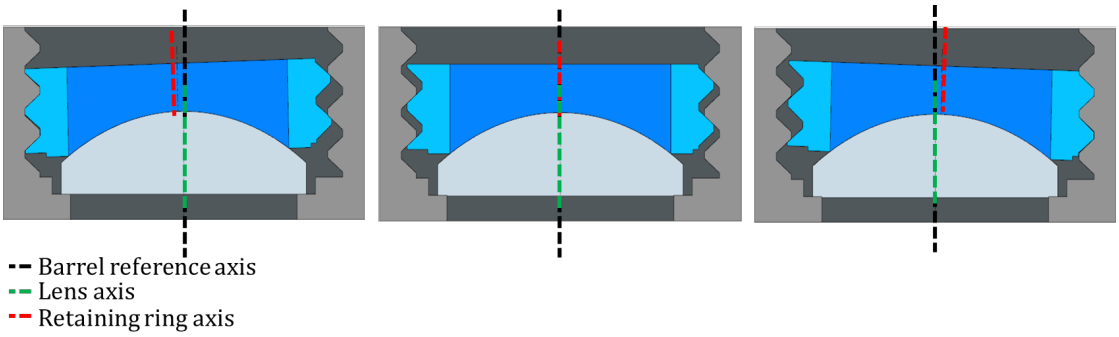

Figure 17: To satisfy the self-centering condition, the thread angle is adjusted accordingly. Notably, the tilt of the retaining ring has no impact on the centering of the lens. Regardless of the tilt, the lens remains centered as long as the self-centering condition is met

The study by Frédéric Lamontagne et al. [46] conducted multiple measurements using the self-centering technique to assess the centering of optical surfaces in contact with a ring. The measurements involved various lens types, including plano-convex, meniscus, and bi-convex lenses,

with different diameters and radii of curvature. The TRIOPTICS OptiCentric MOT 100 was utilized, a centration measurement instrument often seen in assembly processes.

Out of the 121 measurements conducted, the results revealed a mean centering error of 3 μm, with a standard deviation of 1.4 μm. To put this into perspective, when compared to typical barrel designs, which exhibited a mean centering error of 48.9 μm and a standard deviation of 36.1 μm, the self-centering technique demonstrates its potential for significantly improving the centering precision of typical barrel designs.

The self-centering technique can be applied to a wide range of lens shapes, provided that the self-centering criterion is adhered to. However, it is important to note that not all lens shapes are suitable for self-centering. The effectiveness of self-centering relies on its ability to overcome the frictional forces that hinder centering. These frictional forces are influenced by factors such as the clamping angle, normal force, the friction coefficient between the lens and mechanical components, as well as dynamic effects during the assembly of the threaded ring. Merely employing simple calculations with static coefficients of friction would not be sufficient.

Therefore, it is more appropriate to establish a shape criterion for self-centering based on a minimum clamping angle that must be satisfied. Equation 8 presents the mathematical formulation for computing the clamping angle, while Figure 18 showcases several illustrative examples. In the equation, R_1 and R_2 represent the radii of the first and second lens surfaces, respectively, while y_1 and y_2 denote the contact radii of the retaining ring and barrel seat, respectively.

Defining a minimum clamping angle provides a robust criterion for ensuring the success of self-centering, and best reflects the complex interplay of forces and dynamic factors involved in the process. By adhering to this criterion, the reliability and predictability of self-centering are insured, thereby contributing to the overall success of the technique.

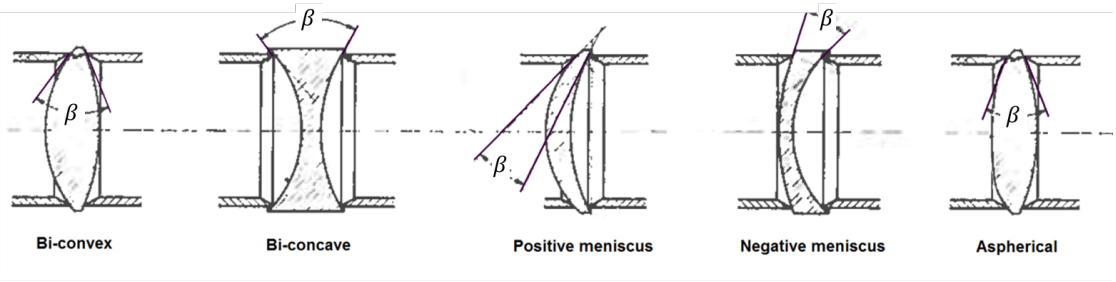

Figure 18: Clamping angle β for different lens shapes [46]

$$\beta = \left| sin^{-1}\left(\frac{y_1}{R_1}\right) + sin^{-1}\left(\frac{y_2}{R_2}\right) \right| \geq 14.0 \text{ degrees} \tag{8}$$

INO, the company holding the patent for the self-centering technique [54], conducted over 200 measurements using three different types of optical coatings and three different types of anodized aluminum. The results of these measurements demonstrated guaranteed success when employing a clamping angle equal to or greater than 14 degrees. Moreover, certain lenses without optical coatings were successfully centered with a clamping angle as low as 7.8 degrees. Further reduction of the clamping angle can be achieved by employing methods such as vibration or the use of lubricants to minimize friction.

Self-centering conditions can be achieved even for designs that fall below the prescribed clamping angle by utilizing the lens edge instead of the lens surface. To accomplish this, the retaining ring is equipped with a spherical surface that interfaces with the lens edge, as depicted in Figure 19. This approach allows for a large clamping angle that is independent of the lens surface's radius of curvature. Such a technique can be applied to cylindrical lenses of any type. Nevertheless, it is important to acknowledge the drawbacks associated with this method. The optical surface of a lens possesses the most stringent tolerances, while the edge of the lens typically exhibits lower precision, thereby introducing a higher margin of error. Additionally, the spherical surface on the retaining ring must exhibit tolerances similar to those of the lens's optical surface to achieve comparable centering precision [51].

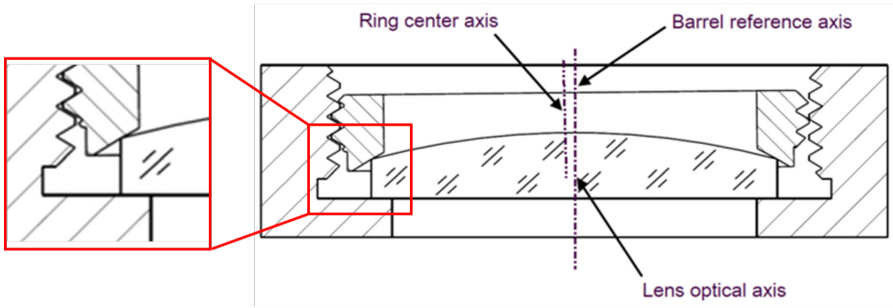

Figure 19: This self-centered edge contact mount utilizes a spherical surface on the retaining ring to achieve self-centering. [51]

To determine the radius of the spherical surface on the retaining ring, Equation 7 can be reformulated to solve for R. The resulting equation is expressed Equation 9.

$$R = \sqrt{\left(\frac{d_{ring}}{2tan\left(\frac{\varphi_{thread}}{2}\right)} - h - \frac{\alpha}{2}\right)^2 + y^2} \tag{9}$$

An alternative approach to address a smaller clamping angle is to introduce a local radius on the lens. This method involves incorporating a specific radius at a particular location on the lens surface. Figure 20 visually depicts this technique, and Equation 9 can be utilized to calculate the necessary radius for achieving self-centering. While this method offers improved tolerance control relative to the edge contact, it places additional demands on the manufacturing process of the lens, requiring precise execution to ensure accurate results.

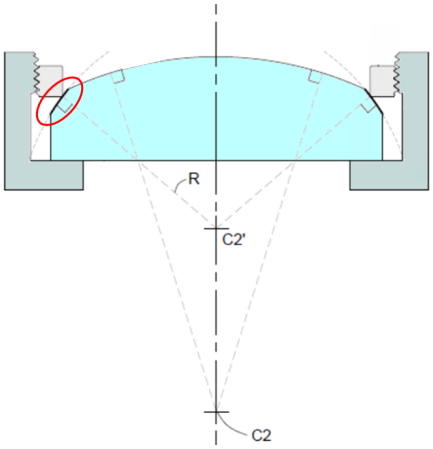

Figure 20: Self-centering can be achieved by introducing a localized radius on the lens, indicated by the red circle. [46]

In conclusion, the concept of self-centering lenses presents a promising solution for improving the centering precision of typical barrel designs in optical instruments. By leveraging the geometrical relationship between lens diameter, lens radius of curvature, and thread angle, self-centering conditions can be achieved, reducing positioning errors and relaxing manufacturing tolerances.

The self-centering technique allows for the elimination or minimization of decentering caused by the clearance in the thread connection between the lens and the barrel. By ensuring that the decentering of the center of curvature of the lens surface in contact with the retaining ring is equal to the decentering of the retaining ring itself, self-centering conditions are met. This enables precise alignment of the lens, even in the presence of dimensional and geometric errors in the lens and mechanical mounts.

The effectiveness of self-centering has been demonstrated through experimental measurements. Compared to typical barrel designs, the self-centering technique exhibited significantly lower centering errors. It is important to note that not all lens shapes are suitable for self-centering. The evaluation of the clamping angle criterion plays a pivotal role in the selection of an appropriate self-centering design.

The self-centering technique holds promise for replacing the existing coupler and collimator mount designs, with the aim of enhancing stability, reliability, and manufacturing tolerances. This paper delves into an investigation of the self-centering method as a mounting design for the collimator and coupler lenses in the ULS. Through this research, a deeper understanding of the capabilities and limitations of the self-centering technique in the context of optomechanical engineering will be gained, fostering advancements in the field.

This research commences by examining the existing mounting design for the coupler and collimator lenses. Subsequently, an optimized self-centering design is proposed as an alternative approach. Simulations are conducted to evaluate the performance and feasibility of the self-centering concepts. Finally, the research culminates in a comparative analysis, resulting in the identification and selection of the optimal mounting mechanism for the ULS. By following this comprehensive approach, a thorough analysis of the self-centering technique as a mounting solution for the coupler and collimator lenses is achieved, combining theoretical assessments, calculations, and computational simulations.

2 Mounting Designs

The coupler and collimator lenses play a vital role in the ULS by facilitating the coupling of the infrared laser to the HCF and the collimation of the resulting supercontinuum light. Once collimated, the supercontinuum light can be directed toward the metrology sensors for further analysis. Both the coupler and collimator lenses are cylindrical in shape, with a diameter ranging from 10 to 13.6 mm. These lenses are equipped with anti-reflective coatings, specifically ranging from 1000 to 1050 nm for the coupler lens and from 350 to 1700 nm for the collimator lens.

The coupler lenses are optically bonded together and can be approximated as a singlet lens system. The configuration of the coupler lens system is illustrated in Figure 21. Lens 1 of the coupler lens system is composed of S-NBM51, an optical glass with a CTE of 6.5 and Young's modulus of 81.7 [55]. On the other hand, Lens 2 is made of N-FK58, another optical glass with a more desirable CTE of 13.7 and Young's modulus of 70 [56].

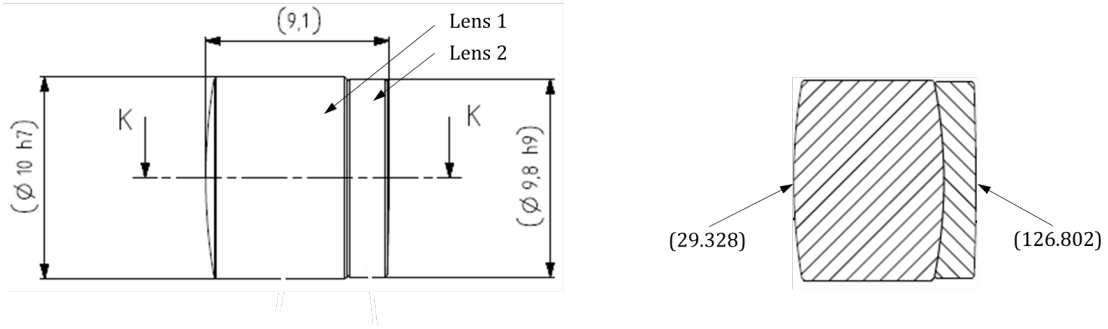

Figure 21: Geometry of the coupler lenses 1 and 2

The collimator lenses are separated by an air gap with a thickness of $0.093 \pm 0.02\ mm$. The geometry of Lens 1 of the collimator lens system is depicted in Figure 22. This lens is composed of N-LAK22, an optical glass with a CTE of 6.6 and Young's modulus of 90 [56].

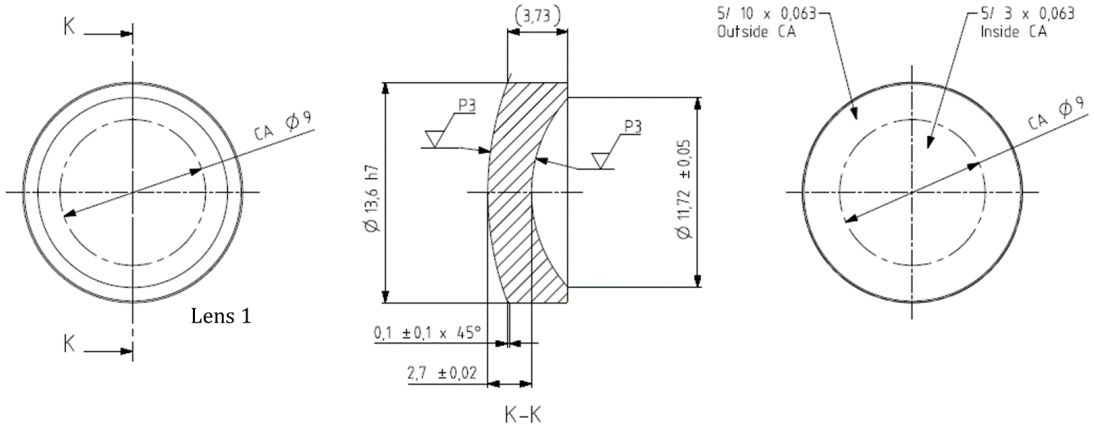

Figure 22: Geometry of the Collimator lens 1

The geometry of Lens 2 in the collimator lens system is shown in Figure 23. Lens 2 is fabricated from N-SF6HT, an optical glass with a CTE of 9 and Young's modulus of 93 [56].

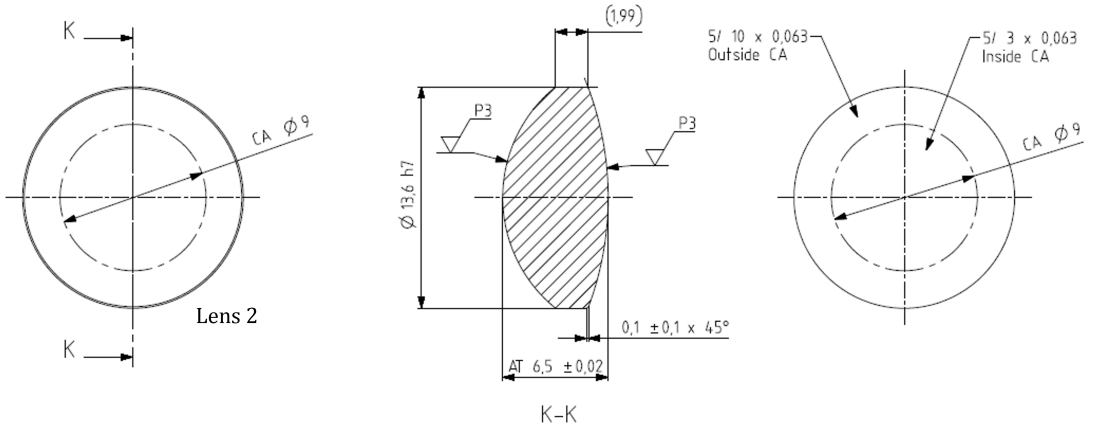

Figure 23: Geometry of the Collimator lens 2

The ULS is presently in the research phase, characterized by ongoing measurements and testing that contribute to the progressive improvements of the coupler and collimator mounts. The existing design of the coupler and collimator mounts serves as a valuable resource for gathering knowledge from past tests and experiments. This knowledge can then be utilized to inform and guide improvements in the development of a new mount design. By leveraging the insights gained from the current design, it becomes possible to refine and optimize the new design, ensuring a more robust and efficient system overall.

2.1 Current Mounting Designs

The coupler and collimator mounts are made of stainless steel 316. The choice of stainless steel 316 as the material for these mounts is based on its relatively high stiffness and low CTE when compared to aluminum. It should be noted that the material selection is not included in the scope of this research paper.

2.1.1 Current Coupler Mount

The current design of the coupler mount, as depicted in Figure 24, utilizes a flexure mount configuration consisting of three flexures. The flexures have a thickness of $0.25mm$ and a conformal contact shape, which poses significant challenges during the manufacturing process. To address these challenges, Wire Electron Discharge Machining (Wire EDM) is chosen as the manufacturing technique. Despite its higher cost, Wire EDM offers tight tolerances within the sub-μm range, making it suitable for realizing this design.

This design prioritizes thermal performance through the implementation of conformal heat transmission across the lens walls. To achieve this, the proximity of metal heat sinks to the lens walls is minimized, enabling efficient dissipation of thermal energy. The thermal center is strategically positioned along the Z-axis to provide stability and resilience against temperature changes, further enhancing the overall thermal performance of the system.

To ensure precise alignment, special assembly tools are designed to center the lens within the mount before securely fixing it using an adhesive. This glass-to-metal connection is achieved through the use of an epoxy resin, which necessitates tight control over the adhesive thickness, bond strength, cure shrinkage, UV resistance, and out-gassing. Recent tests conducted on the ULS have revealed a concerning amount of backscattered UV light, which poses a risk to the adhesive's lifespan. This results in a growing interest in an adhesion-free mounting design.

Recent testing of the ULS has uncovered a substantial amount of UV light that is reflected back toward the coupler mount. This development raises concerns about the long-term durability of the adhesive used in the mounting design. Consequently, there is a growing interest in exploring alternative mounting designs that eliminate the need for adhesives altogether.

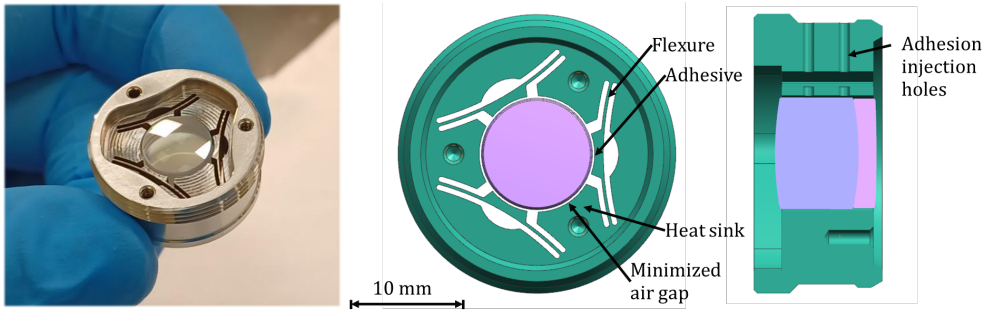

Figure 24: Current coupler mount

2.1.2 Current Collimator Mount

The current design of the collimator mount assembly, as depicted in Figure 25, employs a flexure sub-mount configuration comprising of three flexures. The flexures have a thickness of $0.3mm$ and a conformal contact interface with the lens, rendering wire EDM the most appropriate manufacturing technique for producing these intricate features. To assemble the collimator mount, the sub-mounts are positioned within the main mount body and secured by a retaining ring that firmly clamps the sub-mounts together. Precise alignment is ensured by imposing tight tolerances on the component's interfaces.

The thermal center is strategically positioned along the Z-axis to provide stability and resilience against temperature changes, enhancing the overall thermal performance of the system.

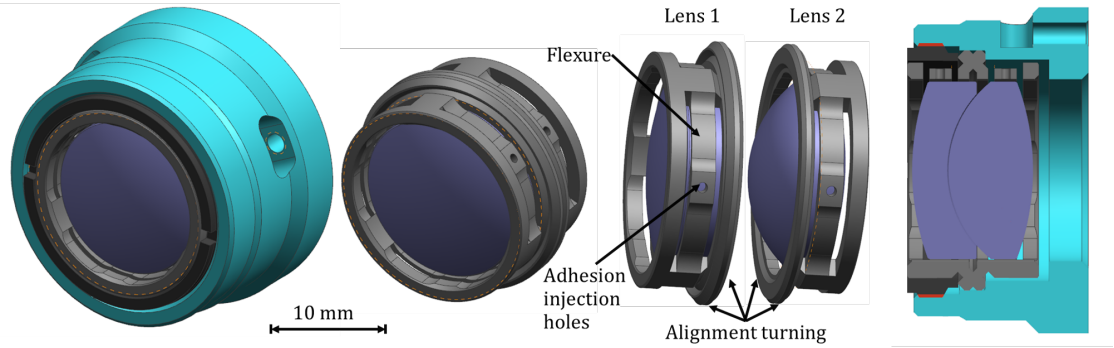

Figure 25: Current Collimator mount assembly consists of the main mount body depicted in blue, the retaining ring in dark gray, and the flexure sub-mount in light grey.

Special assembly tools are specifically designed to achieve initial centering of the lens within the mount before it is permanently fixed using an adhesive. The adhesive used for the glass-to-metal connection is an epoxy resin, which introduces challenges in various parameters such as adhesive thickness, bond strength, cure shrinkage, UV resistance, and out-gassing. Furthermore, the manufacturing process of alignment turning is employed to achieve not only precise alignment of the lenses relative to each other but also accurate alignment relative to the main mount body. This process plays a crucial role in ensuring the accuracy of the lens mount.

Alignment turning is a manufacturing technique that addresses any misalignment that may occur after the lens is mounted. The process, as illustrated in Figure 26, involves several steps. First, the misalignment of the lens assembly is measured. Subsequently, the assembly is oriented to align with the rotational axis of the turning machine. Finally, diamond turning is employed to selectively remove material from the lens mount, thereby correcting the misalignment and ensuring the desired alignment of the lenses.

Figure 26 provides a visual representation of the sequential steps involved in the alignment-turning process, which serves as an effective method of achieving precise alignment of the lenses.

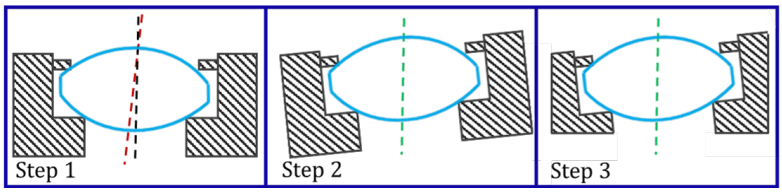

Figure 26: Alignment turning: the process of measuring, aligning, and turning [57]

In recent testing of the ULS, the appearance of carbon growth on the lens surface has been observed, compromising both the performance and lifespan of the lenses. It is hypothesized that this carbon growth is a result of the out-gassing of the epoxy resin. Consequently, there is considerable interest in exploring the self-centering mounting mechanism as an alternative, as it eliminates the reliance on adhesives.

2.2 Self-Centering Advancements

Self-centering has the potential to make significant contributions to the field of lens mounting in optomechanics. However, only a few papers on this topic exist, all written by Frédéric Lamontagne. Therefore, further research to gain a better understanding of self-centering is of great value. This chapter aims to investigate the implications of self-centering for the coupler and collimator mount, using this as a practical case study. By optimizing the self-centering parameter and examining the sensitivity to tolerances, valuable insights can be obtained.

2.2.1 Optimization of Parameters in Self-Centering Mounts

We will commence by analyzing Equation 10 which represents the lateral decentering of the center of curvature of the lens surface in contact with the retaining ring Δ_{tilt} and Equation 11 which represents the self-centering condition. Both equations were introduced in Chapter 1.1.7.

$$\Delta_{tilt} = \left(\sqrt{R^2 - y^2} + h + \frac{\alpha}{2}\right) \frac{2\Delta_{ring} \tan\left(\frac{\varphi_{thread}}{2}\right)}{d_{ring}} \tag{10}$$

$$\Delta_{tilt} = \Delta_{ring} \tag{11}$$

The first noteworthy aspect is the influence of the parameters in this equation. An increase in the radial clearance Δ_{ring}, thread depth α, or distance between the thread and lens h leads to an enlarged centering error. Conversely, increasing the barrel and retaining ring diameter d_{ring} reduces the centering error. The thread angle φ_{thread} is determined by equation Equation 12, introduced in Chapter 1.1.7. Therefore, this parameter cannot be used to minimize potential centering errors.

$$\theta_{ring} = \sin^{-1}\left(\frac{2\Delta_{ring} \tan\left(\frac{\varphi_{thread}}{2}\right)}{d_{ring}}\right) \tag{12}$$

It is important to note that deviating from the standardized radial clearance imposes an additional strain on the manufacturing process, which contradicts the purpose of this self-centering technique. Thus, it is decided to maintain or closely approximate the standardized radial clearance for the new design.

By selecting a value of h equal to $-\alpha/2$, we can eliminate the parameters h and α from the equation. This choice implies that the interface between the lens and retaining ring is located halfway within the thread depth, as depicted in Figure 27.

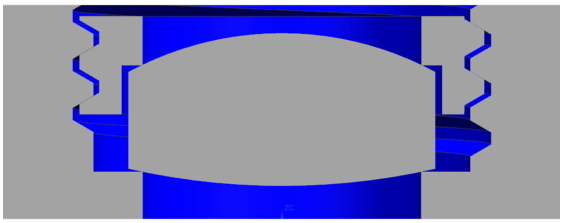

Figure 27: Example of a barrel mount with h equal to $-\alpha/2$

The lens radius R is determined by the optical design and cannot be adjusted to minimize centering errors. However, the contact radius y can be maximized to achieve an improved self-centering configuration, although it is constrained by the lens diameter. When selecting this parameter, it is important to consider the lens clearance and thermal shrinkage.

In order to optimize the self-centering design, it is imperative to deviate from the initial barrel design. To illustrate this, let's consider the second lens of the collimator lenses as an example, with the corresponding parameters provided in Table 1 A. Utilizing Equation 12, we calculate the thread angle to be 0.64 radians or 36.81 degrees. Employing Equation 5, we determine the corresponding thread clearance, denoted as φ_{thread}, to be 0.75 mm.

Table 1: Parameters

A	Variable	Input	Unit
	d_{ring}	15	mm
	R	19.454	mm
	h	1	mm
	α	5	mm
	y	4	mm
	$\varphi_{threads}$	36.81	°
	Δ_{ring}	0.75	mm

B	Variable	Input	Unit
	d_{ring}	30	mm
	R	19.454	mm
	h	-2.5	mm
	α	5	mm
	y	6.5	mm
	$\varphi_{threads}$	78.57	°
	Δ_{ring}	0.31	mm

To account for manufacturing tolerances, we introduce an arbitrary tolerance of 0.1 mm on the variables h and α, -0.1 mm on y and d_{ring}, and 1 degree on φ_{thread}. Evaluating the self-centering condition, we calculate the centering error, as shown in Equation 13. In the ideal scenario where perfect self-centering is achieved, the centering error, represented by Δ_{error}, should theoretically be zero.

$$\Delta_{error} = \Delta_{tilt} - \Delta_{ring} \tag{13}$$

Substituting the values from Table 1 A into the equations, we find that a typical self-centered barrel design results in a centering error of 33.03 μm.

For the purpose to optimize the self-centering design and therefore minimize the centering error, we increase the parameters d_{ring} and y, while setting h to $-\alpha/2$, as shown in Table 1 B. As a result, the thread angle is calculated to be 1.37 radians or 78.57 degrees, and the corresponding thread clearance is reduced to 0.306 mm. Consequently, the resulting centering error is significantly reduced to 7.12 μm. This reduction can primarily be attributed to the decreased thread clearance that is needed for a larger thread angle. despite that, when the thread clearance is maintained at 0.75 mm, the centering error is still reduced to 17.5 μm.

In Figure 28, the influence of the parameters d_{ring}, ranging from 15 to 30 mm, and y, ranging from 5 to 6.5 mm are presented for the collimator and coupler lenses. These ranges adhere to the design boundaries of the mount. Despite lens 2 being a bi-convex lens and lens 1 being considered as a plano-convex lens, the difference in centering error is minimal. This can be attributed to the fact that the radius of the surface in contact with the retaining ring of the collimator lens 1 is only 0.281 mm shorter. Notably, for these particular lenses, the contribution of y to the centering error reduction is negligible, merely amounting to a decrease of sub-0.1 μm.

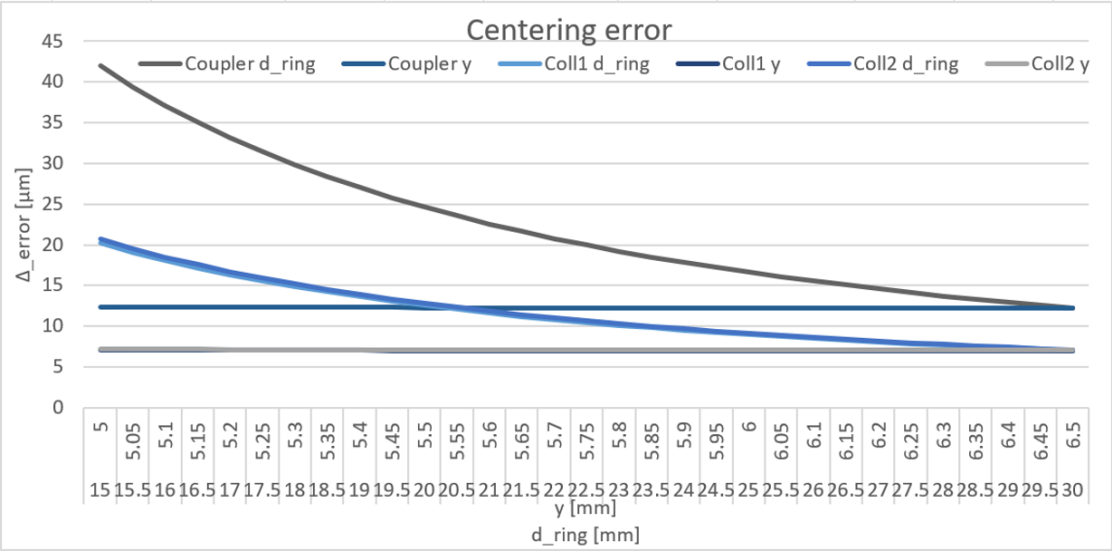

Figure 28: Parameter contribution to centering error in the collimator and coupler lenses

2.2.2 Tolerances Sensitivity of Self-Centering Mounts

Conducting an in-depth analysis of tolerances is a crucial aspect in comprehending the tolerances sensitivity of the self-centering technique. This analysis serves to ensure that the desired optical performance is attained, accounting for all the inherent manufacturing tolerances. In order to execute a comprehensive tolerance analysis, all parameters outlined in Equation 10 are taken into account.

To enhance the effectiveness of the self-centering mount, it is advisable to impose stricter tolerances on parameters that exert a significant influence on the centering error. Conversely, tolerances on parameters with minimal impact on the centering error can be relaxed, thereby striking a balance between manufacturing difficulty and centering performance.

Meaningful tolerance ranges are selected by adhering to the Generic Standard of ASML (GSA) about the manufacturing general geometrical specifications. This document specifies the default dimensional and geometrical tolerances of ASML parts, including tolerances on threads. These specifications are valid for all ASML machined parts unless overruled by specifications on the drawing [58].

To establish the range for tolerance analysis, default tolerances are employed as upper-end values. In this case, a tolerance range of 0 to 0.2 mm is adopted for length parameters, such as d_{ring}, y, h, and α. Additionally, a tolerance range of 0 to 2 degrees is applied for the thread angle (φ_{thread}).

The tolerance range for the lens surface radius (R) is determined by evaluating typical optical fabrication tolerances. It is expressed as a percentage of the radius, where a tolerance of $\pm 0.2\%$ of the radius is employed for lower precision lens surfaces [59].

Initially, the tolerances on the length parameters are examined by introducing a tolerance on each parameter individually. This analysis is performed for both the coupler lenses and collimator lenses 1 and 2. The coupler lenses are treated as a singlet since they are securely cemented

together. Figure 29 presents the centering error of the length parameters for lens 1 (left) and lens 2 (right), while Figure 30 depicts the same for the coupler lenses. A negative error signifies an offset to the left of the barrel reference axis, whereas a positive error corresponds to an offset to the right.

It is noteworthy that the steepness of the line represents the magnitude of the effect a tolerance has on the centering error of a specific parameter. Notably, a tolerance of 0.2 mm results in a maximum centering error of only 3.3 μm, further corroborating the hypothesis that this self-centering technique relaxes manufacturing tolerances.

Consequently, it can be concluded that among these parameters the most effective approach to enhance self-centering precision lies in improving the tolerances of parameters d_{ring} and R.

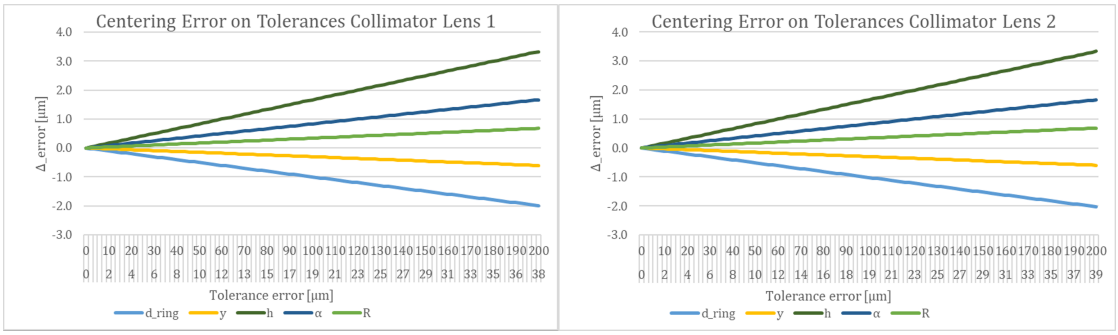

Figure 29: The resulting centering error in collimator lenses 1 and 2 is analyzed as a function of tolerances. Specifically, the tolerances vary within the ranges of 0 to 200μm for parameters d_{ring}, y, h, and α, and within the range of 0 to 38, 39μm for parameter R

When comparing Figures 29 and 30, a notable observation is that the tolerance on the d_{ring} parameter of the coupler lenses exerts a more pronounced influence on the centering error compared to that of collimator lenses 1 and 2. This discrepancy can be attributed to the smaller thread angle associated with the coupler lens surface in contact with the retaining ring.

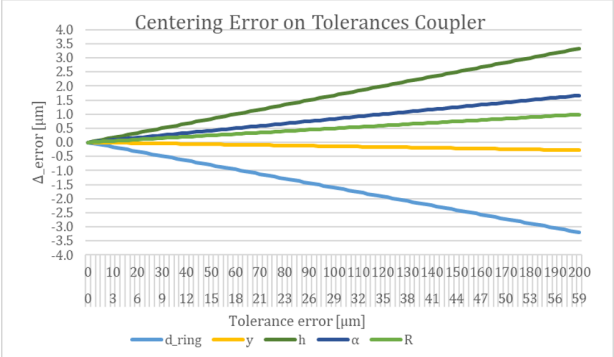

Figure 30: The resulting centering error in the coupler lenses is analyzed as a function of tolerances. Specifically, the tolerances vary within the ranges of 0 to 200μm for parameters d_{ring}, y, h, and α, and within the range of 0 to 59μm for parameter R

Figure 31 illustrates the centering error ranging from 0 to 2 degrees for the coupler and collimator lenses. The tolerance assigned to this parameter significantly impacts the centering error. Hence, it is advisable to align the tolerance of this parameter with the centering requirement to ensure the mount performs as expected. The difference in centering error between the coupler and collimator lenses can be attributed to the smaller thread angle associated with the coupler lens surface in contact with the retaining ring.

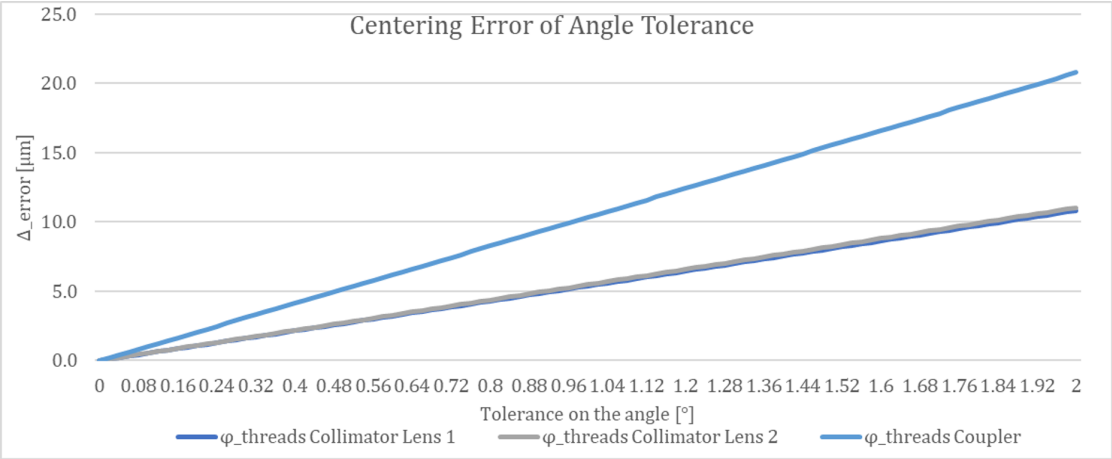

Figure 31: The resulting centering error in collimator lenses 1, 2, and the coupler lenses are analyzed as a function of the angle tolerance. Specifically, the tolerances vary within the ranges of 0 to 2 degrees

In order to comprehensively assess the overall performance and functionality of the system, it is important to consider the statistical behavior of these variations. A Root Square Mean (RSM) analysis provides a statistical approach that facilitates the evaluation of the cumulative effect of dimensional and tolerance variations within a mechanical system or assembly. This method is particularly well-suited for analyzing complex systems with multiple dimensions and tolerances that interact with one another, as it assigns probability distributions to the dimensional variations.

While other methods such as Worst-Case Analysis and Monte Carlo Simulation have their merits, they may be more appropriate in specific situations. Worst-Case Analysis primarily focuses on identifying scenarios where tolerance variations lead to the largest deviations. However, since the mount can be easily loosened and retightened to achieve better centering, this method does not accurately represent the system in the most realistic manner.

On the other hand, Monte Carlo Simulation involves simulating random variations and analyzing their impact on the system. This method assigns probability distributions to each tolerance, representing the expected statistical behavior of the variations. However, since the probability distributions for the tolerances are not known in this context, the Monte Carlo method is not employed here. The RSM method proves particularly effective when dealing with statistical variations and evaluating the cumulative effect of tolerances in this mounting system.

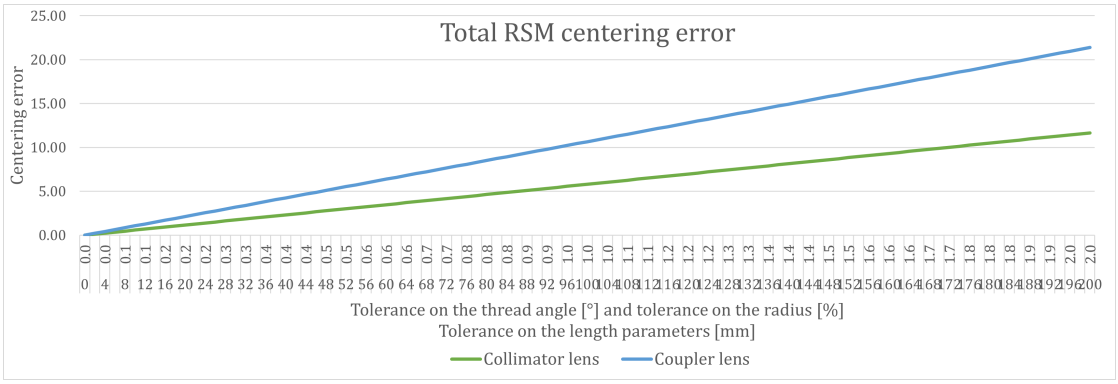

Figure 32: Total RSM centering error curve on increasing tolerances

The tolerance sensitivity of the parameters is greatly influenced by the radius of the surface in contact with the retaining ring. To visualize this relationship, the ratio of the radius to the lens diameter is altered from 1, representing a spherical lens, to 0.3, representing a flatter convex lens. The parameters listed in Table 1 B, with a variable radius ranging from 6.8 mm to 23 mm, are used as input. A tolerance of 0.2 mm is assigned to the length parameters, such as d_{ring}, y, h, and α, a tolerance of 2 degrees is applied to the thread angle (φ_{thread}), and a tolerance of 2% is applied to the radius. Figure 33 visually demonstrates the impact of the radius on the tolerance sensitivity for the different parameters. Upon analyzing the total RSM of the centering error, an optimal ratio of 0.73 emerges.

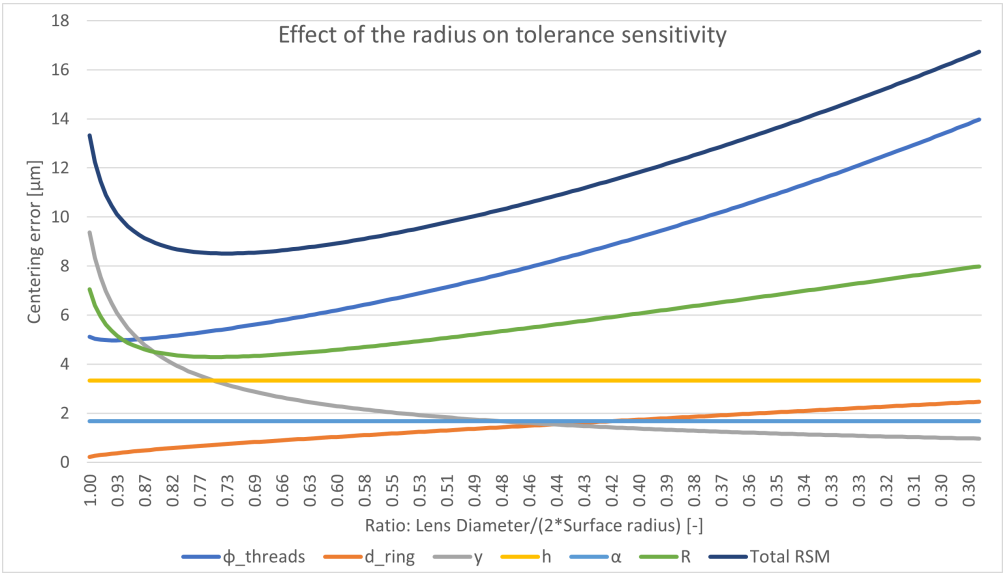

Figure 33: The impact of the radius on the tolerance sensitivity for the self-centering parameters

In the context of a self-centering design, where the lens edge serves as the interface between the retaining ring and the lens itself (see Figure 19), the radius and thread angle can be adjusted to achieve an optimal configuration. It should be emphasized that the tolerances for the contact

radius on the retaining ring are expected to be larger than those for the lens surface radius. Consequently, the contact radius on the retaining ring is subjected to the same tolerance as the length parameters, which are set at 0.2 mm.

The coupler mount, characterized by constant input parameters $d_{ring} = 30$, $h = -\alpha/2$, $\alpha = 5$, and $y = 5$, are subjected to a systematic analysis to determine its optimal configuration. To determine this, a systematic approach is followed whereby the thread angle is incrementally increased from 30 to 165 degrees. In order to satisfy the self-centering condition, the corresponding radius is calculated using Equation 14, which was introduced in Chapter 1.1.7. the resulting graph with a visible optimal point for the coupler lens is shown in Figure 34

$$R = \sqrt{\left(\frac{d_{ring}}{2\tan\left(\frac{\varphi_{thread}}{2}\right)} - h - \frac{\alpha}{2}\right)^2 + y^2} \tag{14}$$

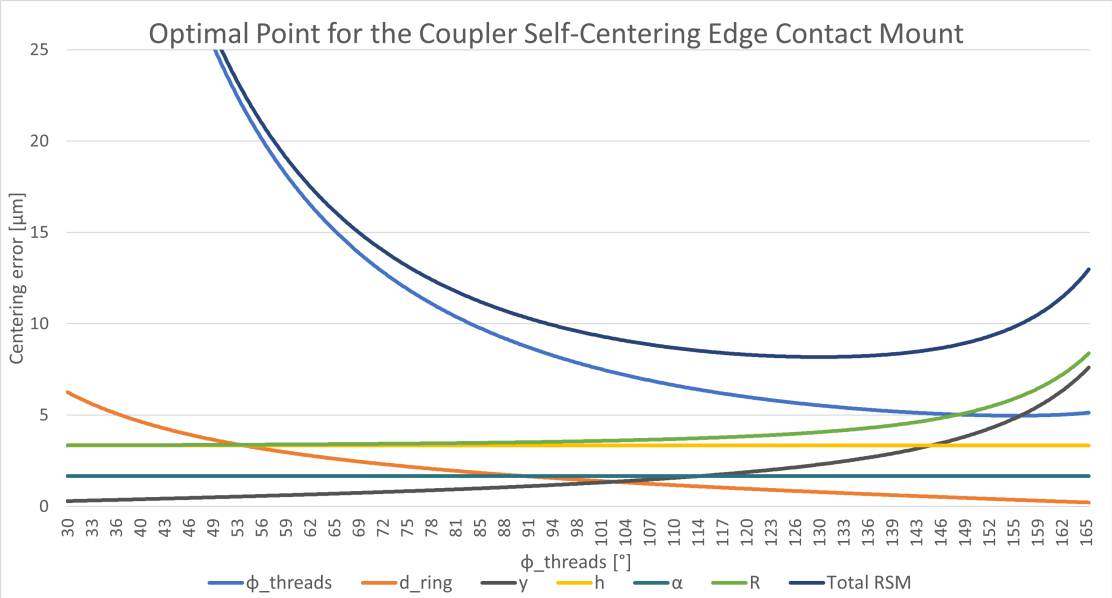

Figure 34: Centering errors for parameters in the self-centering edge contact mount with different radii and complimentary thread angle

After conducting the analysis, an optimum configuration is identified with a thread angle of 130 degrees, resulting in a radius of 8.63 mm. Notably, the parameters d_{ring} and φ_{thread} become less sensitive to tolerances as the thread angle increases and the corresponding radius decreases. Conversely, parameters y and R exhibit the opposite behavior, with their sensitivity increasing. The parameters α and h remain constant throughout this analysis.

2.2.3 Analysis of Sliding and Tipping Behavior

The self-centering method relies on the lens sliding to align with the barrel's reference axis. Sliding occurs when the frictional force between the lens and its mount is lower than the perpendicular force acting on it. To determine whether thick lenses, such as the coupler lenses, will

tip or slide in the mount, one must compare the moments involved in tipping and consider the balance between the applied force and the frictional forces for sliding. Tipping occurs when the tipping moment exceeds the resisting moment, whereas sliding occurs when the applied force overcomes the frictional forces.

The primary factor influencing the sliding behavior in the mount is the friction between the surfaces. Accurately calculating or predicting the friction coefficient is challenging due to several reasons. Firstly, the complex interactions between microscopic irregularities on surfaces make precise measurements or modeling difficult. Secondly, surfaces can vary in roughness, texture, and composition, and even minor changes can significantly affect friction. Thirdly, friction is a nonlinear phenomenon, and the relationship between applied force and frictional force can vary based on factors such as normal force and relative velocity. Additionally, friction is sensitive to environmental factors such as temperature, humidity, and pressure, further complicating predictions. Moreover, simplified models and assumptions are often employed, which may not fully capture the complexity of real-world scenarios. Overall, the interplay of these factors contributes to the challenge of accurately calculating or predicting the friction coefficient. Consequently, this study implements the frictional force as a variable while studying the potential for tipping.

The coupler lenses, which are considered to be a thick singlet, are susceptible to tipping, which may eliminate their self-centering properties. This study utilizes the self-centering edge contact design since it has a higher potential for tipping compared to the typical self-centering design. Initially, the coupler lenses are analyzed in the horizontal orientation, as depicted in Figure 35A. Subsequently, their behavior in the vertical position is examined, as shown in Figure 35B. The vertical position is considered to determine whether the coupler lenses will tip or slide after it is assembled in the ULS.

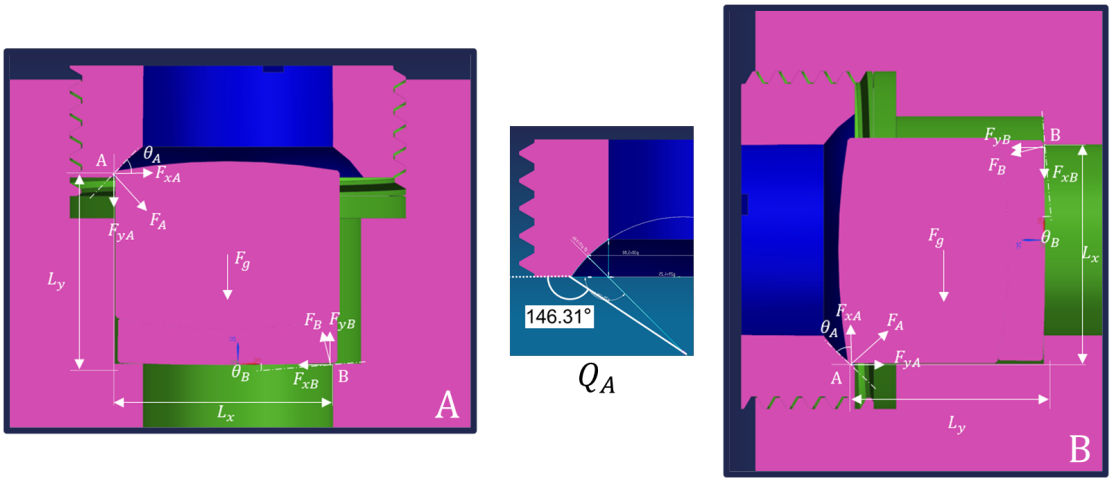

Figure 35: Orientation, parameters, and force schematics of a self-centering edge contact mount. A: Horizontal orientation. B: Vertical orientation.

The tipping force, denoted as F_{Tip}, is calculated using Equations 15 and 17, which involve the calculation of the moment around point B. To find F_{Tip}, the sum of the moments is set to zero, and the tipping force ($F_{\text{Tip}} = F_{\text{xA}}$) is extracted from that equation.

The sliding force, denoted as F_{slide}, is determined using Equations 16 and 18, which involve the

sum of forces in the x-direction equated to zero. The sliding force represents the force required to overcome the frictional force.

$$F_{tip\ horizontal} = (F_{yA} * L_x + F_g * L_{xc})/L_y \tag{15}$$

$$F_{slide\ horizontal} = (F_{yA} + F_g) * cos(\theta_B) * \mu \tag{16}$$

$$F_{tip\ vertical} = (F_{yA} * L_x + F_g * L_{yc})/L_y \tag{17}$$

$$F_{slide\ vertical} = F_{yA} * cos(\theta_B) * \mu \tag{18}$$

Figure 36 presents the sliding and tipping forces as functions of the friction coefficient. When the tipping force exceeds the sliding force, the lens will slide. Conversely, when the tipping force is lower than the sliding force, the lens will tip. Since the friction coefficient cannot be accurately represented by a single value but rather by a range, error bars are included in the graph. Upon comparing both graphs in Figure 36, it can be observed that the lens will slide in its horizontal position if the friction coefficient is below 0.44. However, when the mount is vertically oriented, the lens will always slide because the gravitational force does not contribute to the frictional force.

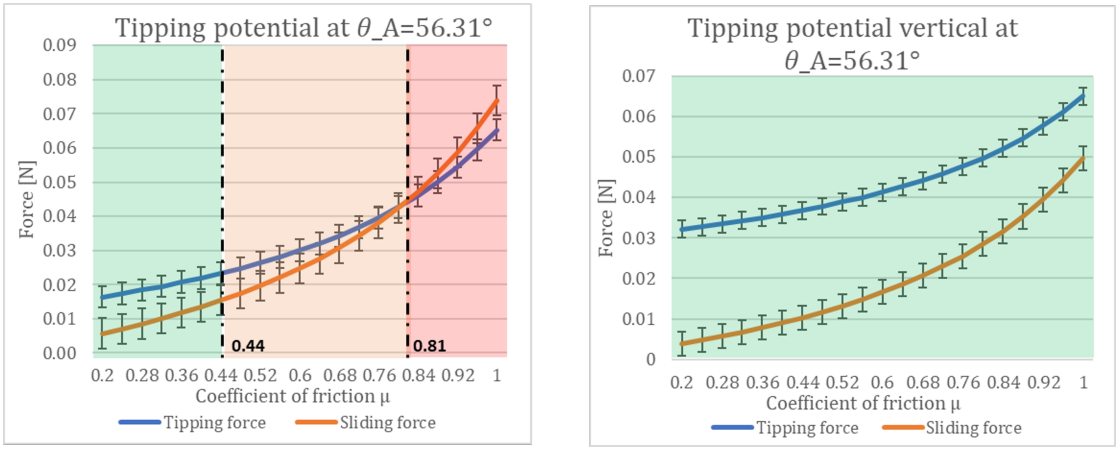

Figure 36: Tipping potential for the coupler lenses in a self-centering edge contact mount. (Left) Horizontal orientation. (Right) Vertical orientation.

Estimating the precise values of the friction coefficient between stainless steel and optical lenses or anti-reflective coatings presents a significant challenge. However, through empirical data and rough approximations, the friction coefficient between stainless steel and optical glass can generally be expected to fall within the range of 0.2 to 0.5. These values are based on experimental data and are provided as rough estimates, an example is shown in Figure 37. It is important to note that the actual friction coefficient can vary due to specific material properties, surface conditions, and other influencing factors.

	fused silca on stainless steel																
[mm]	L	500															
[mm]	H	220	140	95	185	135	110	115	115	110	115	180	115	125	140	165	160
[°]	α	23.7	15.6	10.8	20.3	15.1	12.4	13.0	13.0	12.4	13.0	19.8	13.0	14.0	15.6	18.3	17.7
[-]	cof	0.41	0.27	0.19	0.35	0.26	0.22	0.23	0.23	0.22	0.23	0.35	0.23	0.24	0.27	0.32	0.31

Figure 37: Coefficient of friction (cof) measurements between fused silica and stainless steel

2.3 Mounting Concepts

When designing the new coupler and collimator mounts, several aspects need to be taken into account to ensure proper functionality, compatibility, and reliability. Special considerations must be made in terms of stability, thermal effects, alignment, and manufacturability. Alignment and manufacturability are provided by the self-centering method. We start by evaluating the clamping angle of the coupler and collimator lenses with Equation 19, which was introduced in Chapter 1.1.7.

$$\beta = \left| sin^{-1}\left(\frac{y_1}{R_1}\right) + sin^{-1}\left(\frac{y_2}{R_2}\right)\right| \geq 14.0 \text{ degrees} \tag{19}$$

The cemented coupler lens has a clamping angle of 11.6 degrees, collimator lens 1 has a clamping angle of 18.9 degrees, and collimator lens 2 has a clamping angle of 65.4 degrees. Since the coupler lens has a clamping angle below 14 degrees, the method of self-centering with the lens edge as the interface will be applied to the coupler lens mount. furthermore, the collimator mount will be made with the typical self-centering concept.

By iteratively optimizing the mount's self-centering parameters, the lens can be precisely positioned and aligned to mitigate any manufacturing deviations, leading to improved optical performance. This is done by maximizing the d_{ring} and y while setting h to $-\alpha/2$. The space claim limits the barrel and retaining ring diameter d_{ring} to a maximum of 30 mm. This is to not be in conflict with other parts or modules. The radius of the contact circle y is limited by the radius of the lens and the maximal clearance that the lens has inside the barrel before it is secured. Since the collimator lenses have a radius of 6.8 mm and need a radial clearance inside the barrel of 0.5 mm to fit easily within the barrel without strict tolerances, a 6.3 mm radius is optimal. The radius of the contact circle y of the coupler lenses is bound to its radius and is therefore 5 mm.

The clamping force employed to secure the lens within the mount plays a crucial role in ensuring the stability and reliability of the system. It should provide a strong and reliable grip to prevent any slippage or shifting of the lens during operation or transportation. At the same time, there is a minimum clamping force required to overcome the friction caused by the lens weight, allowing for self-centering to occur effectively.

However, it is important to strike a balance in determining the clamping force. While a certain minimum clamping force is necessary to facilitate self-centering, exceeding this force by a significant margin should be avoided. Excessive clamping forces can introduce additional stresses within the lens, which can adversely affect the refraction of light rays and the state of polarization. Consequently, this can diminish the overall efficiency of supercontinuum generation by reducing the conversion efficiency.

The specific value of the minimum clamping force required for self-centering to occur can be found in Figure 38, providing guidance for determining the appropriate clamping force.

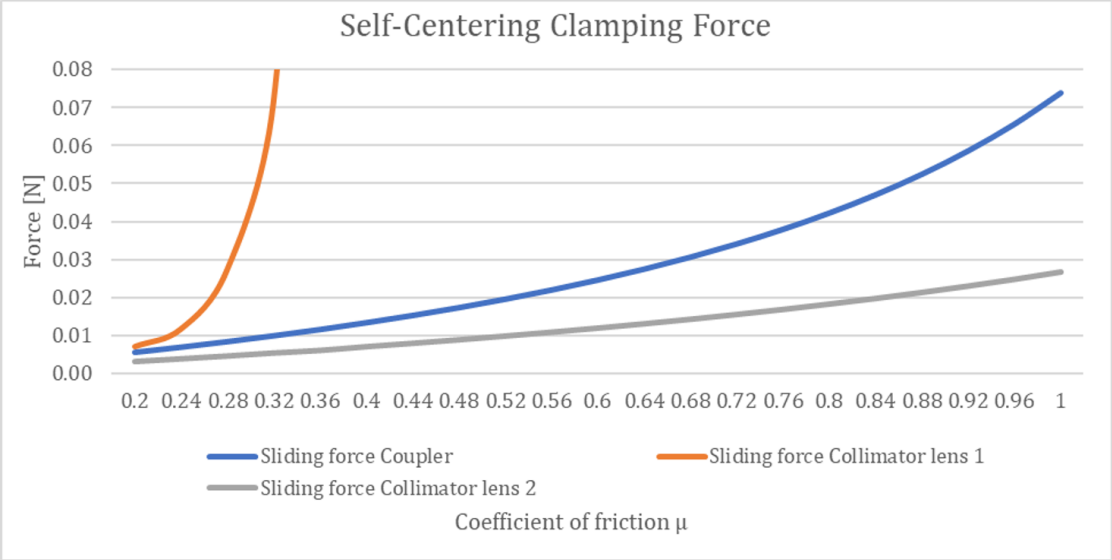

Figure 38: Force needed to achieve self-centering in the coupler and collimator lenses

The clamping force contributes to the friction force that needs to be overcome to self-center the lens. Since the clamping angle of the collimator lens 1 is only 18.9 degrees, a maximal friction coefficient of 0.342 emerges. Larger friction coefficients may pose a risk to the self-centering success. However, this is an overly simplified calculation where in the practical case, due to the rotational motion and additional factors that have an effect on the friction force, it may differ.

The lens mount should be designed with a robust and rigid structure to provide high stability to the lens. This can be achieved by designing a mount that is very solid and provides little to no flexibility. The stiffness of the mount can be evaluated by calculating the natural frequency. The higher the natural frequency is the higher the stiffness of the mount. However, Temperature fluctuations can cause thermal expansion or contraction, potentially affecting the lens performance or worse, resulting in fractures or failure of the lenses. lens fracture or cracks nearly always occurs under tensile stresses in areas where grinding and polishing processes have left small subsurface cracks (often invisible) that are nucleation sites for subsequent fractures. Factors such as the size, direction, and position of the subsurface cracks differ between the even same lens type. For this reason, it is challenging to predict the resistance to tensile stress of each lens.

Transportation poses the requirement to withstand temperature variation of $-25°C$ to $60°C$. Additionally, during operation, the coupler lenses absorb a small amount of the infrared laser. The collimator lenses absorb a small amount of the outgoing supercontinuum. This results in irregular thermal loads that introduce increased contact stresses.

The incorporation of effective thermal management techniques plays a pivotal role in minimizing the detrimental effects of temperature fluctuations. By strategically implementing measures such as local flexibility, a strategically positioned thermal center, or even active cooling mechanisms, the impact of temperature changes can be significantly mitigated.

To ensure optimal optical performance, it is imperative to introduce local flexibility when the tensile stresses arising from temperature variations during operation surpass 0.5 MPa. Failure to address this issue can lead to the emergence of birefringences, ultimately compromising the overall optical performance of the system.

Similarly, transport conditions must also be taken into account, as they can potentially give rise to tensile stresses exceeding 7 MPa. In such instances, it becomes crucial to implement local flexibility as a means of safeguarding the integrity and functionality of the mount.

In designing the mounts careful considerations are made in terms of radial symmetry. This symmetry helps minimize aberrations, which are deviations from ideal optical behavior that can degrade image quality. By maintaining symmetry, aberrations can be reduced or eliminated, leading to better image quality. Symmetrical design is a double-edged sword since it also places the thermal center in the middle of the lenses. The need for a thermal center in the middle of the lens is evident since this provides the highest thermal stability and optical performance. It facilitates constant position under temperature fluctuations.

Additionally, manufacturing on this scale presents several unique challenges compared to larger-scale manufacturing processes. The dimensions and tolerances of components must be accurate within fractions of a millimeter. Inspecting and ensuring the quality of components on this scale can be difficult. Standard inspection methods may not be sufficient, and specialized equipment or techniques are often necessary. Detecting defects, such as surface imperfections or deviations from the desired dimensions, becomes more challenging at such a small scale.

Figure 39 illustrates the three proposed concepts for mounting the collimator lenses. The primary objective is to attain maximal mounting stiffness while ensuring that the tensile stress levels remain below the prescribed threshold of 7 MPa, in accordance with transportation requirements.

The optimized self-centering parameters are utilized in combination with a thermal center in the center of the lenses. The first concept, Concept 1, has the highest stiffness without any flexibility for thermal expansion or contraction. This is optimal for stability but might result in high tensile stresses. Concept 2, incorporates statically placed flexibility to relieve some of the thermal-induced stresses. The flexibility is statically chosen in the z-direction since it is less sensitive to an error in that direction. Concept 3, provides even more flexibility in the case that Concept 2 still results in high tensile stresses. Manufacturing is increasingly more challenging with Concept 1 being the most easy and Concept 3 the hardest.

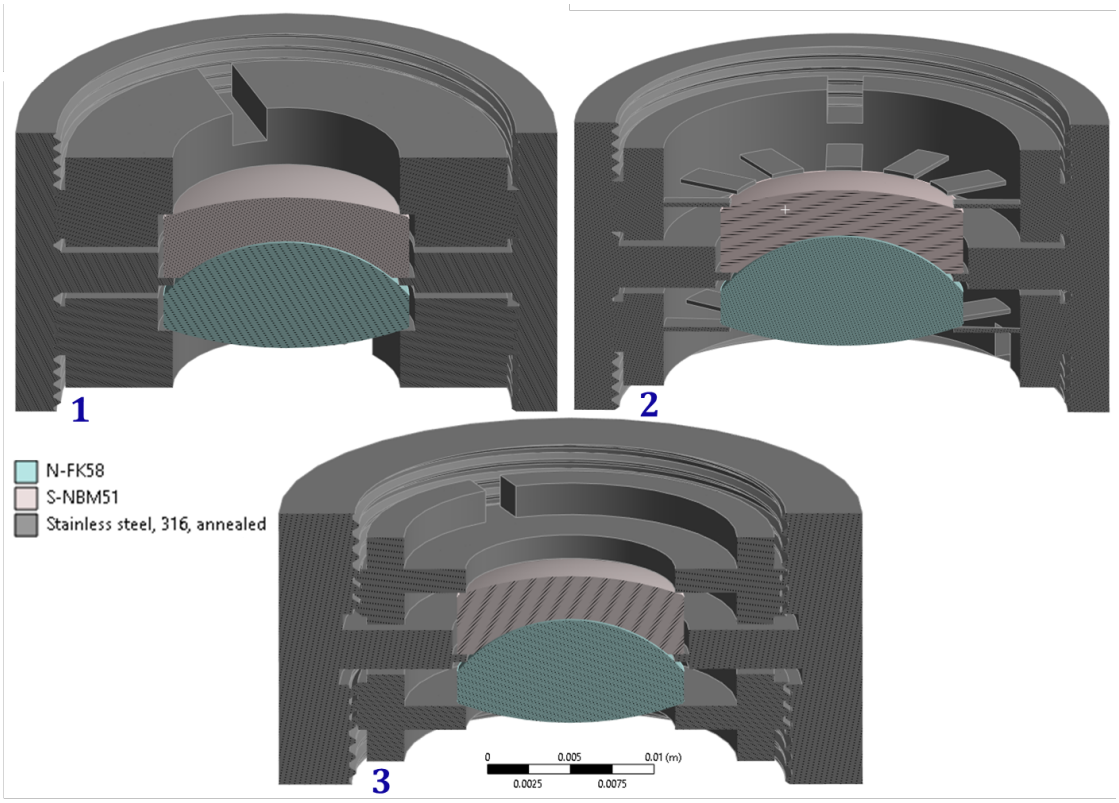

Figure 39: Collimator mount concepts 1, 2, and 3

Figure 40 presents the proposed concepts for mounting the coupler lenses. The primary objective of the different concepts is to attain maximal mounting stiffness while ensuring that the tensile stress remains below the specified threshold of 7 MPa, in adherence to transportation requirements.

Additionally, the optimized self-centering parameters are employed in conjunction with a thermal center located at the center of the lenses. The concepts explored for the coupler mount are similar to those considered for the collimator mount. However, due to the requirements of accommodating thermal expansion and contraction, the coupler mount necessitates a higher degree of flexibility. Consequently, the concept involving a solid retaining ring will not be pursued as it is predicted to be too restrictive. It is important to highlight that the manufacturing process for the coupler mount poses greater challenges compared to that of the collimator lens. This is mainly due to the edge contact method, which requires a relatively smooth surface texture on the contact radius of the retaining ring to ensure proper functionality.

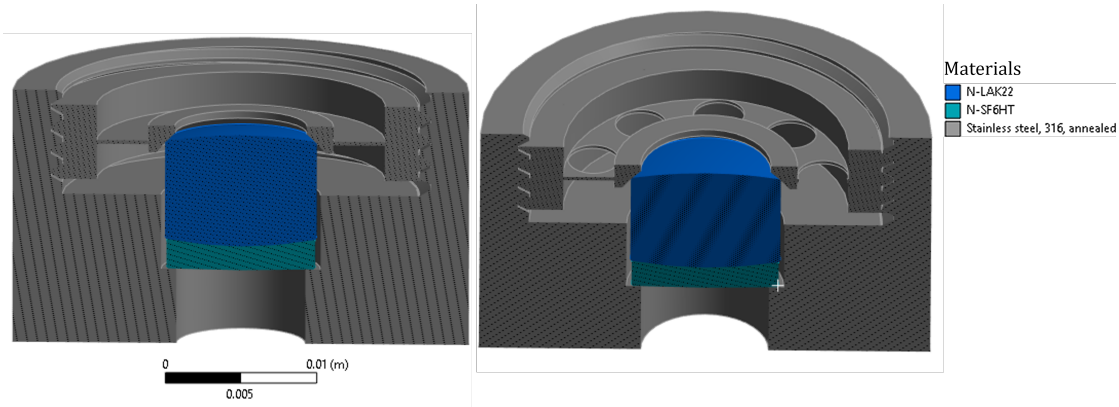

Figure 40: Coupler mount concepts 1, 2, and 3

3 Simulations

ANSYS Workbench 2022 R2, a Finite Element Method (FEM) simulation software, serves as the analytical tool to assess the stress, thermal effects, and eigenfrequency characteristics of the mount and lenses. This software provides a wide range of analysis capabilities, enabling the study of structural and system behavior under operating and transport conditions.

The analysis comprises three distinct types: Steady-State Thermal Analysis, Static Structural Analysis, and Model Analysis. The Steady-State Thermal Analysis predicts temperature distributions and heat flow within the lens and mount, specifically under steady conditions. This analysis aids in determining the maximum temperature reached during operation, thereby assessing the mount's capability to remove heat from the lenses.

To account for the partially restricted airflow, a convection coefficient of $5W/m^2°C$ is applied to the surfaces in contact with air, assuming an ambient temperature of 22 °C. This choice of convection coefficient is based on early tests of the ULS, which have demonstrated that it best represents the environmental conditions in which the ULS is situated.

Furthermore, Static Structural Analysis serves as a fundamental technique to evaluate the structural response of the mount to static loads. It enables the assessment of stress distribution within the lenses resulting from thermal effects experienced during transportation. During transportation, the mount must withstand temperature fluctuations ranging from $-25°C$ to $60°C$. Since the mount has a higher CTE compared to the lenses, it contracts more than the lenses when the temperature drops to $-25°C$. Consequently, this leads to higher contact stresses that may potentially result in fractures or cracks. In this analysis, the evaluation revolves around ensuring that the stresses remain below the specified tensile stress threshold of 7 MPa. Moreover, this analysis is expanded to assess the operational stresses and ascertain their compliance with the established threshold of 0.5 MPa. It is crucial to emphasize that, within the context of the simulations, positive stresses denote tensile stresses, whereas negative stresses indicate compressive stresses.

Additionally, Model Analysis is conducted to evaluate the mount's behavior based on mathematical models that represent its physical characteristics. This analysis technique proves to be a powerful tool for predicting the eigenfrequency, which allows for an evaluation of the stiffness characteristics of each mount.

Through the implementation of these simulation techniques, different design concepts can be explored, enabling a deeper understanding of system behavior. Subsequently, informed decisions can be made based on the comprehensive results derived from the analyses.

A mechanical mesh is established for the mounts, and careful consideration of mesh parameters is crucial to obtain accurate results, making it a vital step in the simulation setup. It is worth noting that reducing the mesh size enhances accuracy and increases computational costs. The accuracy of the results depends on both discretization error and solution error. Discretization error arises from the fact that a given mesh is a discrete approximation of the space, and therefore, it can only provide an approximate solution even when equations are solved exactly.

To determine the optimal mesh size, a mesh independence study was conducted. In this study, the mesh size was progressively decreased until the calculated results exhibited minimal changes. The resulting mesh size, which possesses adaptive sizing, a slow transition, and a resolution of 3 out of 5, was considered optimal. The quality and inflation parameters were kept at their default settings. For surfaces with interactions between parts and surfaces experiencing flexibility, a relatively smaller mesh size was employed, while areas without such characteristics were maintained at the default mesh size. This approach was chosen to optimize computational efficiency while still ensuring accuracy.

The mesh size varies depending on the type of analysis being conducted. For steady-state thermal analysis, a default mesh is employed. In static structural analysis, emphasis is placed on the mesh size of interfaces and flexible parts. In model analysis, smaller mesh sizing is applied specifically to the flexible parts.

Simulations of the current coupler and collimator mount will serve as a reference to evaluate the performance of the self-centering design relative to the current design. The assessment will consider the operating temperature, maximum principal stress, and eigenfrequency as performance indicators.

3.1 Current Collimator Mount

The simulation steps for the collimator mount involve importing the collimator mount into Ansys DesignModeler, a software tool used for creating and modifying 3D CAD models. Once the collimator mount is imported, the next step is to define the necessary boundary conditions in Ansys Mechanical. This includes applying fixed supports and environmental conditions. Additionally, contacts between different components of the mount, such as the lenses and the mounting surfaces, are specified to accurately represent their interaction.

Furthermore, heat loads are applied to simulate the effects of absorbed supercontinuum light and the resulting thermal expansion within the mount. These heat loads represent the thermal energy absorbed by the lenses and are crucial for assessing their impact on the structural behavior of the collimator mount.

3.1.1 Steady-State Thermal Analysis

The supercontinuum light undergoes partial absorption by the lenses, leading to the generation of heat. To simulate this heat load, an internal heat load is introduced to the region illuminated by the light on the lenses. The shape of this area is cylindrical, with a diameter of $1mm$, corresponding to an area of $2.12mm^3$ for lens 1 and $5.10mm^3$ for lens 2. Using the software program Zemax OpticStudio, the expected heat load is calculated to be $9.74mW$ for lens 1 and $5.33mW$ for lens 2.

Lens 1 and Lens 2 establish a connection with the mount through surface contacts, which are subject to program-controlled thermal conductivity. Notably, The presence of a 0.093mm air gap between the lenses warrants careful consideration of the heat transfer that occurs between them. This minimal separation enables a noticeable heat transfer between the lenses. Considering the atmospheric pressures at play, the thermal conductivity of air in such a narrow gap is estimated to be approximately 0.0026 mW/K.

The simulation indicates that the maximum temperature in the lenses reaches $25.2°C$, as depicted in Figure 41. The temperature profile exhibits a relatively uniform distribution around the optical axis, which is desirable for optimal performance. Although the epoxy resin establishes a good thermal connection with the lenses, thereby minimizing the presence of air between the adhesive and the lens, the thermal conductivity of the adhesive is significantly lower than that of stainless steel. Moreover, due to the thin flexure of $0.3mm$, heat flow is constrained, resulting in heat dissipation from the lens to be diminished.

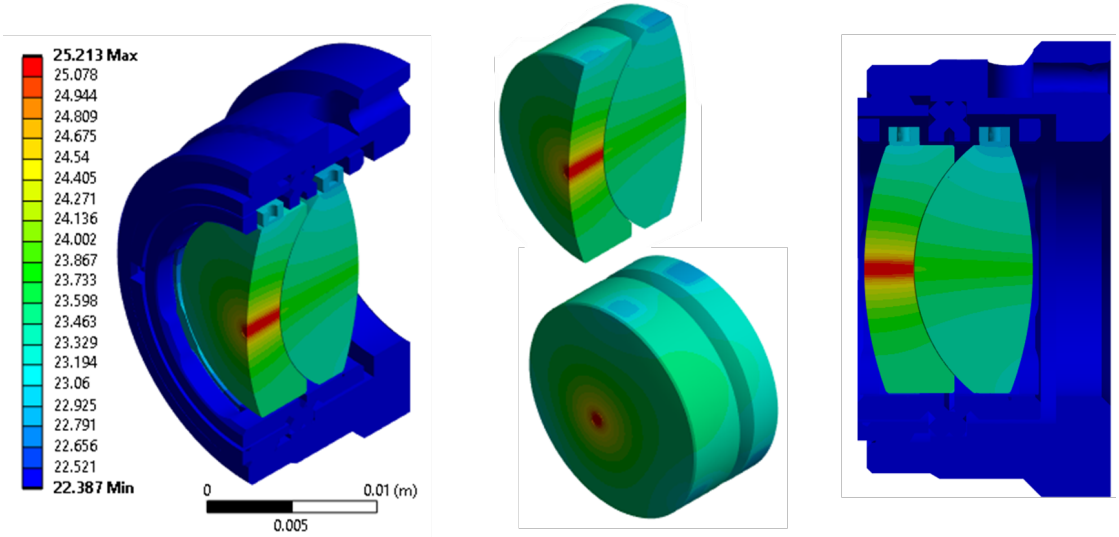

Figure 41: Operating temperature in the current collimator mount

3.1.2 Static Structural Analysis

The operational heat load leads to differential expansion between the lenses and flexures compared to the mount. This differential expansion, caused by the temperature gradient and CTE mismatch among the various materials, induces internal stresses. However, due to the small geometry and a temperature gradient of only $3.1°C$, the resulting stresses are relatively low compared to those experienced during transport. Detailed analysis, as depicted in Figure 42, reveals that the highest calculated contact stress is a mere 0.28 MPa in tension. Furthermore, it is worth noting that higher stress values are observed in the center of the lenses, which can be attributed to the temperature gradient within the lenses themselves.

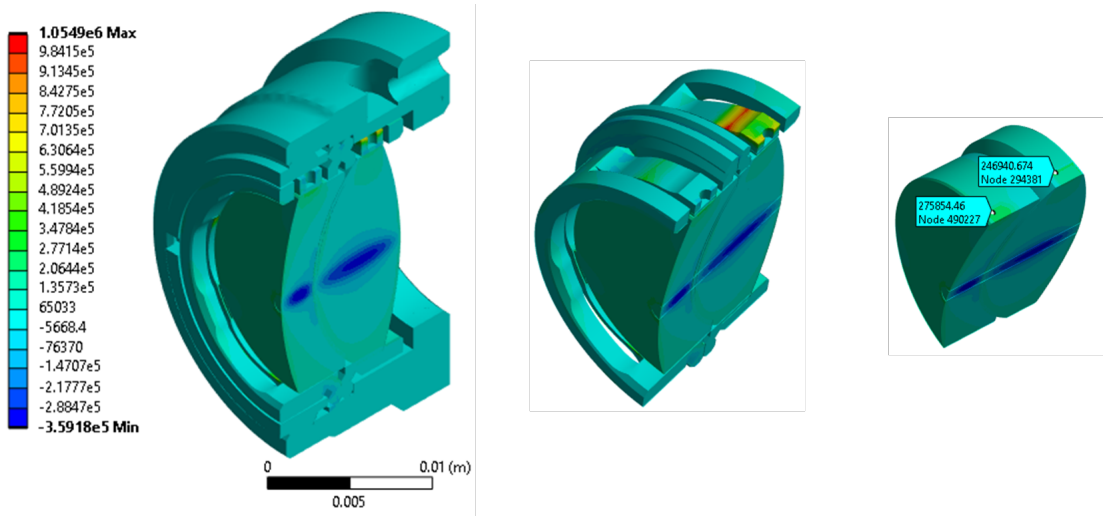

Figure 42: Stresses in the current collimator lenses under operational heat load

The collimator mount and lenses experience a mismatch in CTE, leading to the development of maximal principal tensile stress and compressive stress within the lenses during transport conditions. As depicted in Figure 43, the calculated values for maximal principal tensile stress and compressive stress are 7.56 MPa and 3.72 MPa, respectively. Notably, these values exceed the specified requirement of 7 MPa.

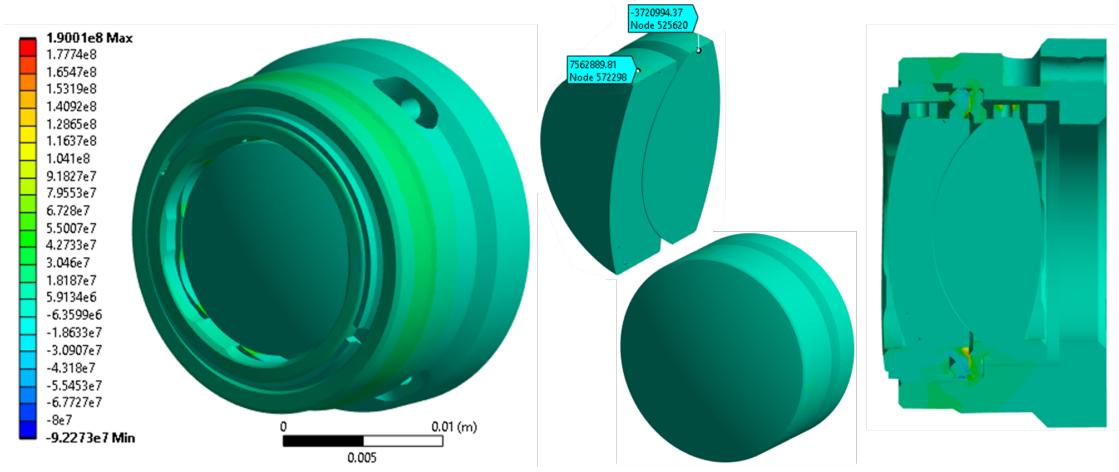

Figure 43: Principal stresses in the collimator mount resulting from a temperature decrease from $22^{\circ}C$ to $-25^{\circ}C$

The elevated stresses arise due to the bonded connection between the collimator mount and the lenses, where sliding is strictly prohibited. However, it is important to acknowledge that the adhesive materials used in practice exhibit viscoelastic behavior, which enables stress relaxation to a certain extent.

The accurate prediction or simulation of stresses in adhesive connections is challenging due to various factors, including intricate material behavior, non-linear deformation, stress distribution and boundary conditions, manufacturing variations, multiple failure modes, and limited experimental data. Adhesive materials, demonstrate viscoelasticity and non-linear stress-strain relationships, further complicating the modeling process. Addressing these challenges requires the application of advanced numerical techniques, experimental validation, and a comprehensive understanding of adhesive behavior.

3.1.3 Model Analysis

Figure 44 illustrates the first six eigenfrequency modes of the current collimator mount. Among them, an eigenfrequency mode of 9.1 kHz is observed in the z-direction, aligned with the optical axis. This particular mode does not adversely affect the performance as it does not result in an alignment error and falls within the optical field of view. However, it is crucial to emphasize that eigenfrequency modes resulting in translations in the x- and y-directions, as well as rotations around the x- and y-axes (modes 1, 2, 3, and 4), have the potential to induce alignment errors. Therefore, it is essential for these modes to possess higher eigenfrequencies relative to other modes. By increasing the eigenfrequencies of these modes, the system's susceptibility to alignment errors can be minimized, ensuring the desired optical performance. Notably, the sixth mode, with a frequency of 19.5 kHz, corresponds to rotation around the optical axis. Due to the symmetrical design of the mount, this mode does not impact the optical performance.

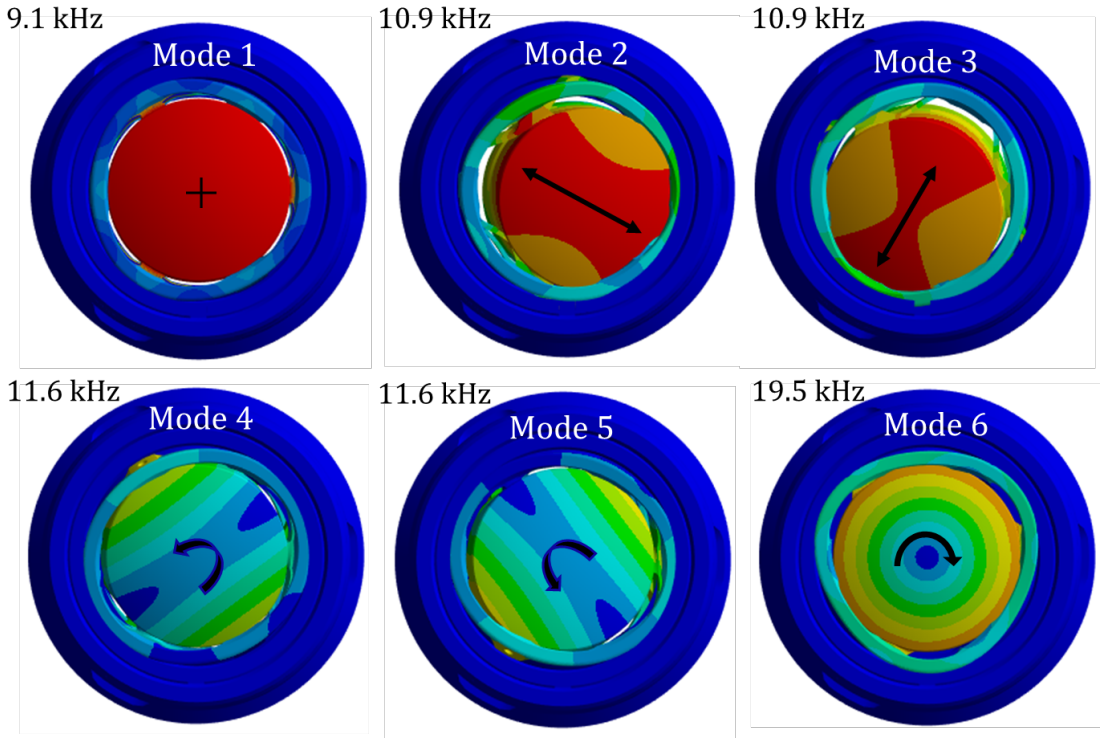

Figure 44: First six eigenfrequency modes of the current collimator mount

3.2 Current Coupler Mount

The current procedure for simulating the coupler mount involves several sequential steps. Firstly, the coupler mount is imported into Ansys DesignModeler. Once imported, the subsequent step entails defining the essential boundary conditions within Ansys Mechanical. These boundary conditions comprise fixed supports and environmental considerations. Moreover, it is necessary to specify the contacts between distinct components of the mount, such as the lenses and the mounting surfaces, in order to accurately represent their interaction.

In addition, heat loads are applied to emulate the effects of absorbed infrared laser radiation and the consequent thermal expansion within the mount. These heat loads serve to replicate the thermal energy absorbed by the lenses, and their inclusion is vital for assessing the impact on the structural behavior of the coupler mount.

3.2.1 Steady-State Thermal Analysis

The infrared laser experiences partial absorption by the lenses, leading to the generation of heat. To simulate this heat load, an internal heat load is introduced to the region illuminated by the light on the lenses. The shape of this area is cylindrical, with a diameter of $2.5mm$, corresponding to an area of $36.7mm^3$ for lens 1 and $7.92mm^3$ for lens 2. Using the software program Zemax OpticStudio, the expected heat load is calculated to be $56.3mW$ for lens 1 and $7.90mW$ for lens 2.

The simulation results reveal that the lenses reach a maximum temperature of $27.5°C$, as depicted in Figure 45. Notably, the temperature profile exhibits a relatively uniform distribution around the optical axis, which is desirable for achieving optimal performance. Despite the adhesives establishing a robust thermal connection with the lenses and minimizing the presence of air gaps, the thermal conductivity of the epoxy resin is significantly lower than that of stainless steel. Additionally, the thin flexure of $0.25mm$ restricts heat flow, resulting in reduced thermal dissipation capabilities.

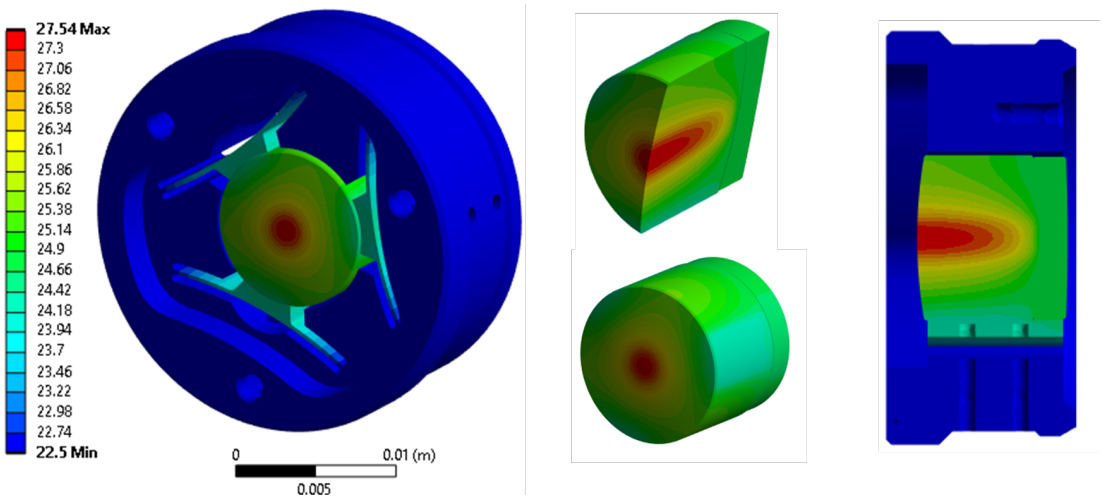

Figure 45: Operating temperature in the current coupler mount

3.2.2 Static Structural Analysis

The presence of the operational heat load gives rise to differential expansion between the lenses and flexures in contrast to the mount. The temperature gradient and CTE mismatch among the various materials induce internal stresses. Notably, due to a temperature gradient of $5.0°C$, the resulting stresses are comparatively elevated in relation to the collimator lenses. The analysis, as illustrated in Figure 46, reveals that the maximum calculated contact stress in tension is 0.82 MPa. Additionally, it is pertinent to observe that the stress values in the central region of the lenses are minimal, owing to the more gradual temperature gradient experienced by them. Moreover, the stresses present in the lenses exceed the specified threshold of 0.5 MPa, thereby adversely affecting the performance of the lenses.

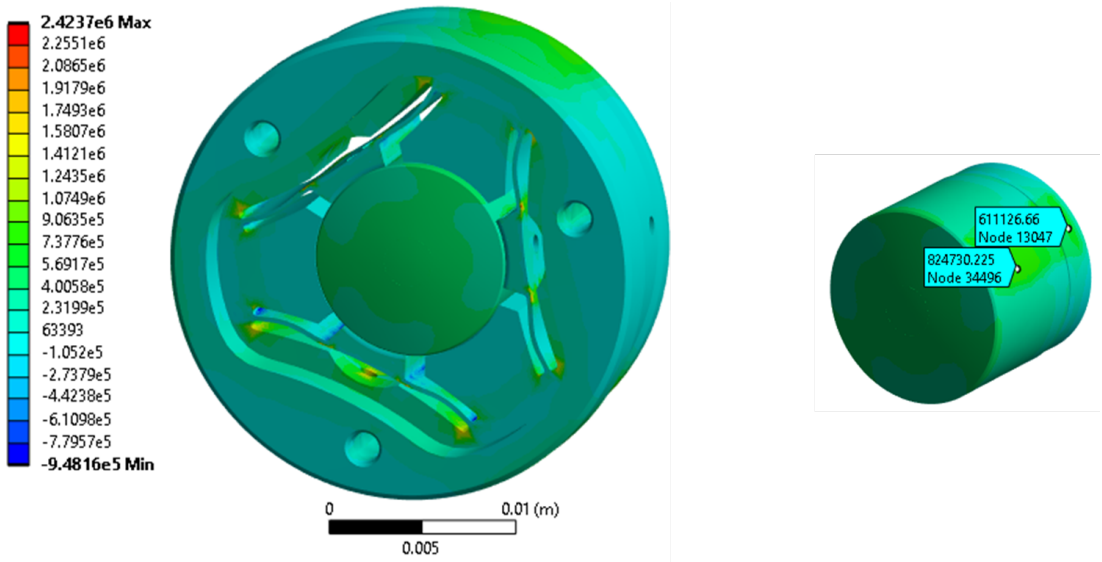

Figure 46: Stresses in the current coupler lenses under operational heat load

The discrepancy in the CTE between the coupler mount and the lenses results in maximal principal tensile stress and compressive stress within the lenses during transport conditions. As shown in Figure 47, the maximal values are measured at 16.73 MPa for tensile stress and 3.01 MPa for compressive stress. These stress levels significantly exceed the specified requirement, indicating a potential risk to the success of this design. furthermore, the challenges associated with accurately predicting and simulating stresses in adhesive connections also persist in the current coupler mount. These challenges contribute to the observation of large stresses in the simulation. This uncertainty poses additional risks to the overall success of the design.

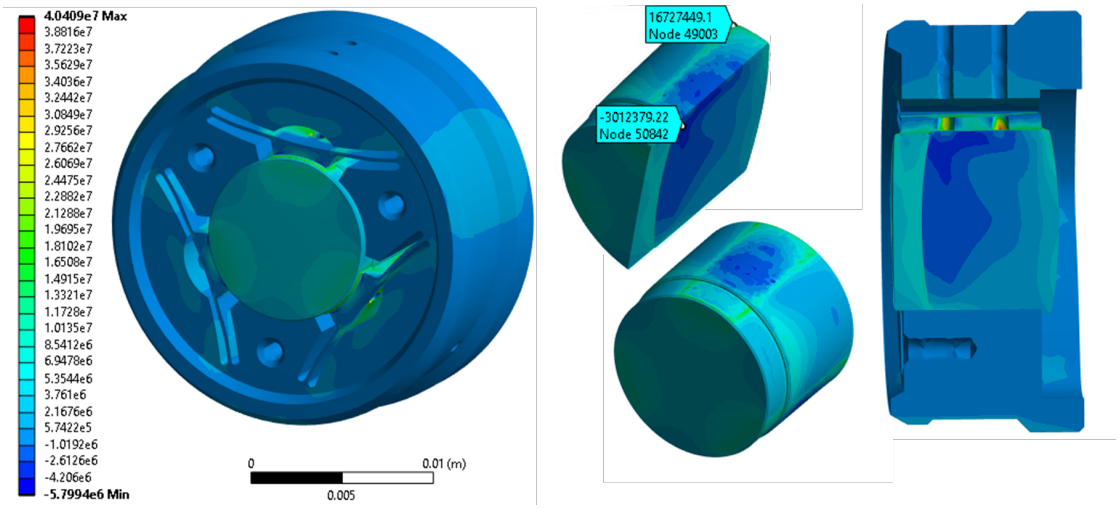

Figure 47: Principle stresses in the current coupler mount resulting from temperature decrease from $22°C$ to $-25°C$

3.2.3 Model Analysis

Figure 48 provides a visualization of the first six eigenfrequency modes of the current coupler mount. Modes 1, 2, 3, and 4 correspond to translations in the x- and y-directions, as well as rotations around the x- and y-axes.

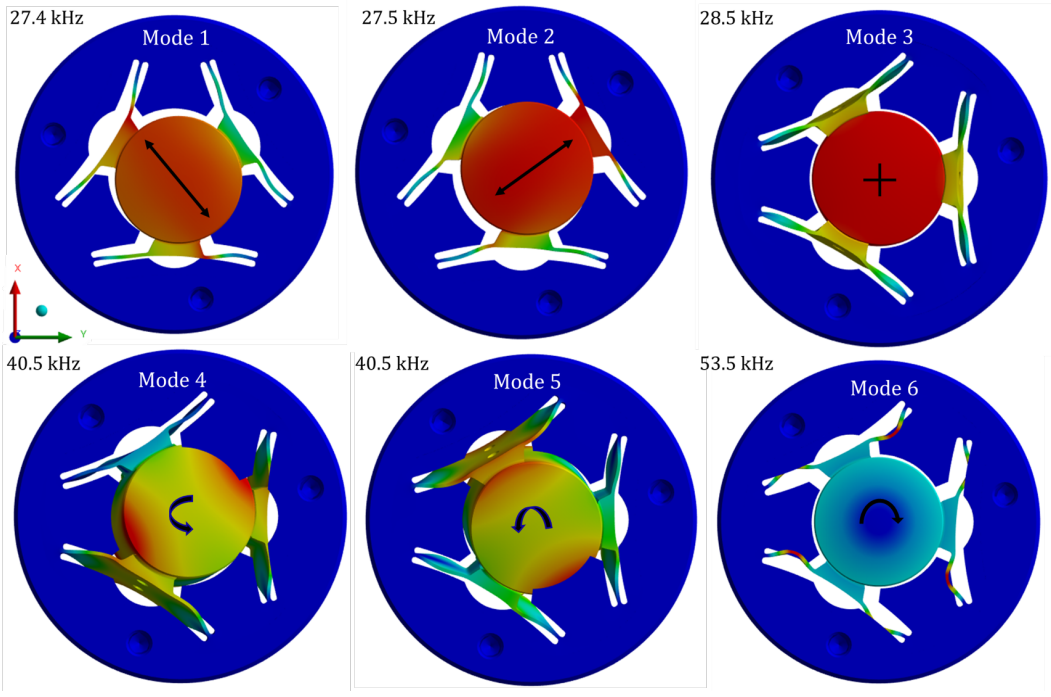

Figure 48: First six eigenfrequency modes of the current coupler mount

These modes possess the potential to induce alignment errors if the mount is excited at those frequencies, thereby adversely affecting the optical performance. To mitigate this, the eigenfrequencies relative to other modes can be increased. It is worth noting that among the observed eigenfrequency modes, there is an eigenfrequency of 28.5 kHz in the z-direction and an eigenfrequency of 53.5 kHz corresponding to rotation around the optical axis. Importantly, these modes do not have a detrimental effect on the optical performance of the mount. Their presence does not induce alignment errors or introduce any significant deviations that could compromise the system's functionality. Therefore, these eigenfrequency modes can be considered as non-critical in terms of their impact on the overall optical performance of the mount.

It is worth mentioning that the coupler mount exhibits significantly higher stiffness compared to the collimator mount. This increased stiffness can be attributed to factors such as the presence of cemented lenses, larger thickness, and smaller diameter of the lenses. These design characteristics enhance the constraint of the system, resulting in higher overall stiffness.

3.3 Self-Centering Collimator Mount

The simulation procedure for the self-centering collimator mount involves several steps, including importing various concepts and defining boundary conditions, fixed supports, environmental conditions, and contacts. The iterative process of fine-tuning the thickness and dimensions of the flexible components is carried out, with careful consideration given to manufacturability while adhering to the core concept. The subsequent chapters present the final iteration of the three concepts.

3.3.1 Steady-State Thermal Analysis

To simulate the steady-state thermal analysis, the collimator lenses are subjected to the same thermal load resulting from the partially absorbed supercontinuum. Lens 1 is connected to the mount through a line contact, while Lens 2 is connected through a surface contact and two line contacts. The thermal conductivity of these contacts is program controlled. Furthermore, a frictionless contact is established between lenses 1 and 2 to account for the air gap, enabling significant heat transfer between the lenses. The thermal conductivity of air at atmospheric pressures with a 0.093mm gap is approximately calculated as 0.0026 mW/K.

The simulation outcomes demonstrate that in concept 1, the lenses reach a maximum temperature of $23.82°C$ as depicted in Figure 49. It is noteworthy that the temperature distribution around the optical axis is relatively uniform due to the centrally located thermal center in the design. The solid retaining ring acts as an effective heat sink, contributing to the reduction of the maximum temperature. Lens 1 exhibits relatively better heat dissipation compared to Lens 2 due to the presence of a surface contact that facilitates increased heat dissipation.

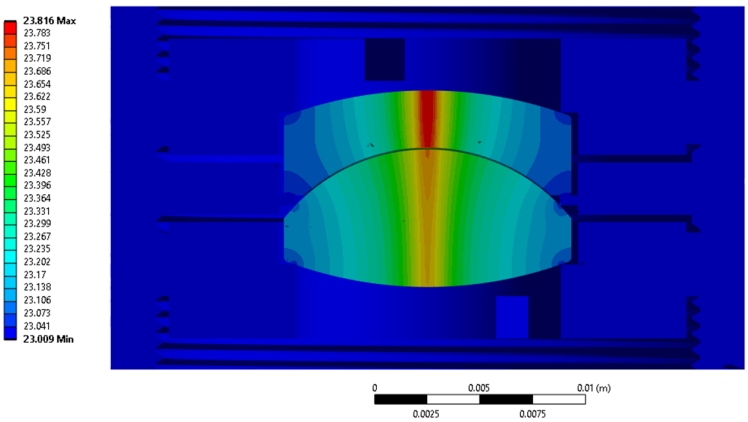

Figure 49: Operating temperature in concept 1 of the collimator mount

The simulation results indicate that in concept 2, the lenses attain a peak temperature of $24.32°C$, as illustrated in Figure 50. Although the flexible component measures a mere 0.25mm in thickness, it does not experience significant temperature elevation due to the sufficient convection that can occur in its vicinity.

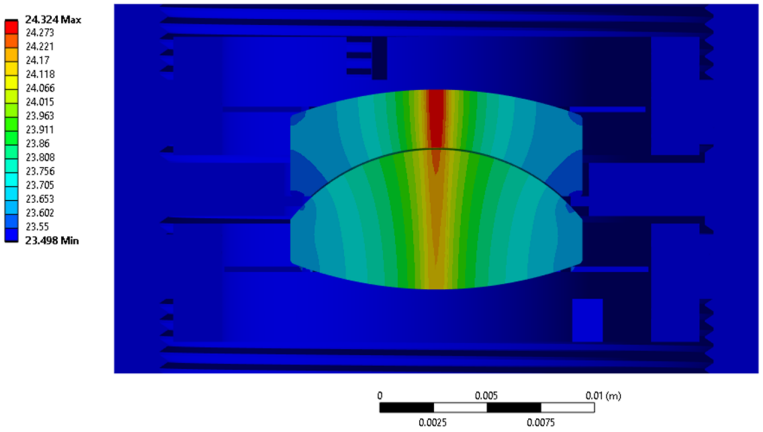

Figure 50: Operating temperature in concept 2 of the collimator mount

The simulation results indicate that in concept 3, the lenses attain a peak temperature of $23.92°C$, as illustrated in Figure 50. The flexible component measures a solid disk of 1.5 mm in thickness. The increased solidity of the flexure, in contrast to concept 2, enables it to effectively dissipate a higher amount of heat. Nevertheless, the absence of airflow caused by the solid disk limits convection within the flexure system. These opposing effects counterbalances, resulting in no substantial temperature disparity when compared to concept 2.

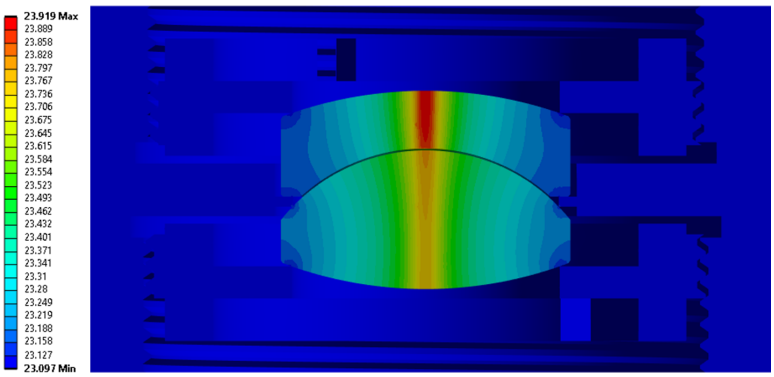

Figure 51: Operating temperature in concept 3 of the collimator mount

3.3.2 Static Structural Analysis

The observed discrepancy in the CTE between the coupler mount and the lenses gives rise to significant principal tensile and compressive stresses within the lenses if the temperature decreases to $-25°C$. The respective maximum values, as depicted in Figure 52, amount to 12.5 MPa for tensile stress and 38.8 MPa for compressive stress. The magnitudes observed in this study significantly exceed the prescribed maximum allowable limit of 7 MPa in tension. Therefore, there is a significant probability that the lenses will crack or fracture during transport.

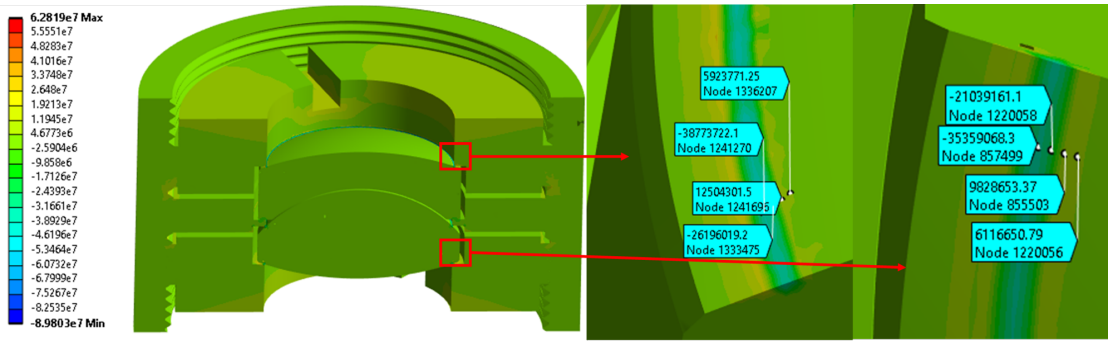

Figure 52: Principle stresses in concept 1 of the collimator mount

The magnitudes of the maximal principal tensile and compressive stresses of concept 2, as illustrated in Figure 53, are recorded as 0.55 MPa and 1.63 MPa, respectively. It is worth noting that both values fall significantly below the prescribed maximum allowable limit of 7 MPa.

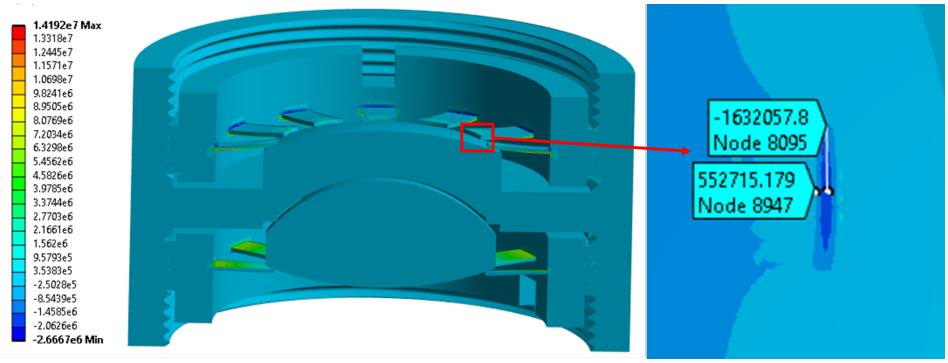

Figure 53: Principle stresses in concept 2 of the collimator mount

The magnitudes of the maximal principal tensile and compressive stresses exerted on the lenses in concept 3, as depicted in Figure 54, have been calculated to be 5.78 MPa and 8.00 MPa, respectively. These values fall within the prescribed threshold of 7 MPa in tension, indicating compliance with the specified requirement while ensuring a satisfactory safety factor.

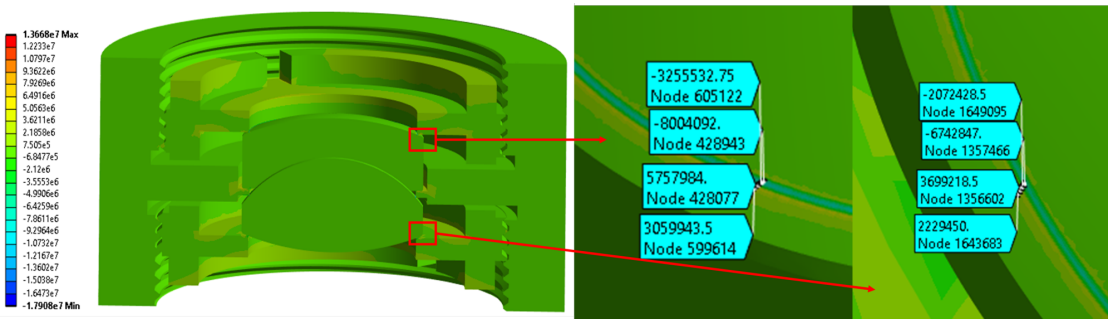

Figure 54: Principle stresses in concept 3 of the collimator mount

3.3.3 Model Analysis

Figure 55 illustrates the first three eigenfrequency modes of the first concept, offering a visual representation of their characteristics. Notably, Mode 2 exhibits a rotational frequency of 58.2 kHz around the y-axis, while Mode 3 demonstrates a similar rotational frequency of 58.6 kHz, albeit with a slight tilt along the y-axis. These two modes possess the potential to introduce alignment errors, thereby exerting a detrimental impact on the optical performance if the mount is excited at those frequencies. In contrast, the first mode manifests as a translational frequency of 37.5 kHz in the z-direction. Consequently, its influence on the overall optical performance of the mount can be deemed non-critical.

It is worth emphasizing that the concept underlying this mount is exceedingly robust and solid, a fact that is further substantiated by the resulting high eigenfrequency modes.

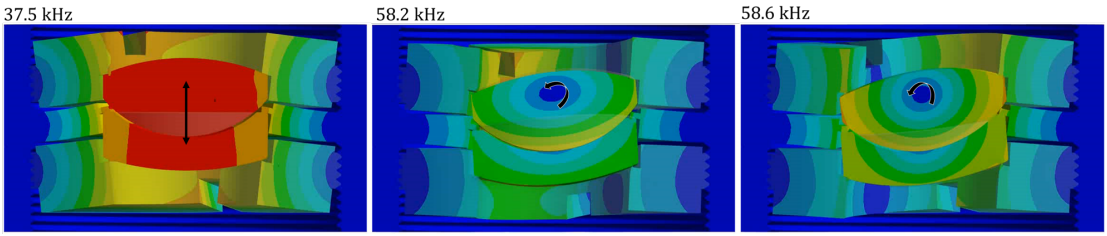

Figure 55: First three eigenfrequency modes of concept 1 of the collimator mount

The first three eigenfrequency modes of the second concept are depicted in Figure 56. These modes provide a visual representation of their respective characteristics. It is noteworthy that the modes share similar frequency directions as concept 1, except for the third mode which exhibits a rotational frequency around the x-axis of 40.8 kHz. In a manner reminiscent of concept 1, mode 1 and mode 2 exhibit similar frequency directions. Both systems exhibit translational frequency in the z-direction and rotational frequency around the y-axis. Nevertheless, this concept demonstrates a reduced frequency compared to concept 1, with specific values of 27.8 kHz and 40.7 kHz for the first and second modes, respectively. It is important to emphasize that despite the thinness of the flexures in this design, it still demonstrates a significant level of stiffness. This can be attributed to the fact that the flexures have a length of only approximately 4 mm.

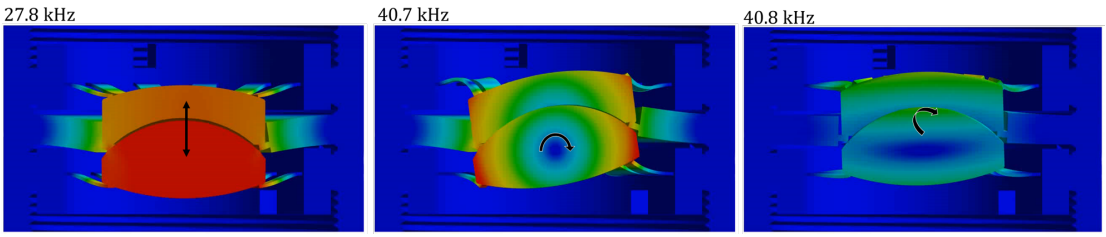

Figure 56: First three eigenfrequency modes of concept 2 of the collimator mount

The first three eigenfrequency modes of the third concept are illustrated in Figure 57. These modes offer a visual representation of their respective characteristics. It is noteworthy that these modes exhibit similar frequency orientations as those observed in concept 2. Specifically, the first three modes are associated with translational motion in the z-direction and rotational motion around the x- and y-axes, with eigenfrequencies of 32.7 kHz, 50.7 kHz, and 51.0 kHz, respectively. However, it should be noted that this concept demonstrates elevated eigenfrequencies compared to concept 2.

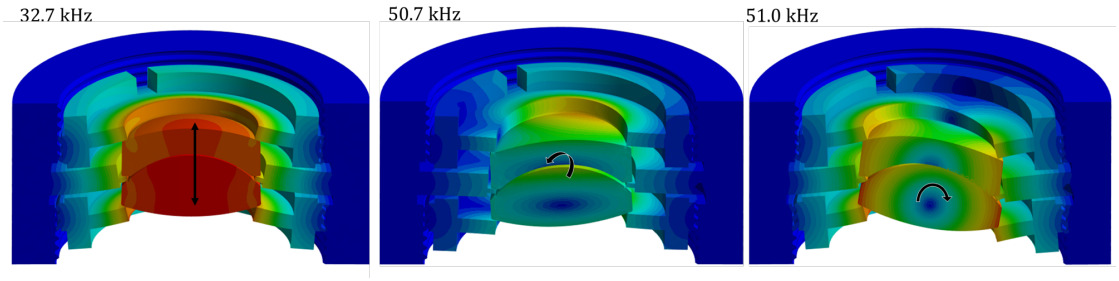

Figure 57: First three eigenfrequency modes of concept 3 of the collimator mount

It is worth emphasizing that all the self-centering collimator mounting concepts exhibit significantly greater stiffness when compared to the current collimator mount. Consequently, these concepts lead to a more stable mounting of the lenses.

3.4 Self-Centering Coupler Mount

The simulation procedure employed for the self-centering coupler mount encompasses a series of steps that entail the incorporation of diverse concepts and the establishment of boundary conditions, fixed supports, environmental conditions, and contacts. An iterative process is then initiated to meticulously adjust the thickness and dimensions of the flexible components, ensuring that manufacturability is taken into account while maintaining fidelity to the underlying principle. The forthcoming chapters will present the final iteration of the two conceptual designs.

3.4.1 Steady-State Thermal Analysis

In order to conduct a comprehensive analysis of the steady-state thermal behavior, it is essential to subject the coupler lenses to the same thermal load generated by the partially absorbed infrared laser. The cemented lenses are connected to the mount through two line contacts, and the thermal conductivity of these contacts is program controlled.

According to thermal analysis in Figure 58, the lenses attain a maximum temperature of $29.9°C$. However, it is important to note that the average temperature of the second lens is significantly lower than that of the first lens. Consequently, this temperature differential may give rise to heightened stresses at the interface of lenses 1 and 2. Notably, the solid barrel employed in this system acts as an efficient heat sink, thereby contributing to the reduction of the temperature in the second lens.

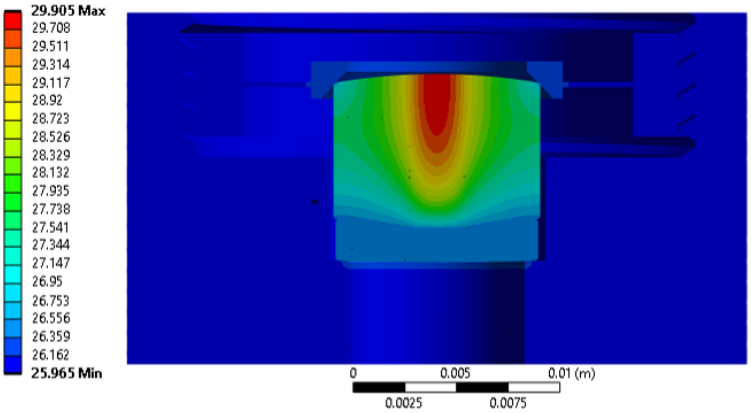

Figure 58: Operating temperature in concept 1 of the coupler mount

Through thermal analysis, as illustrated in Figure 59, it is observed that the lenses reach a peak temperature of $29.5°C$. The presence of holes in the flexible retaining ring facilitates thermal conduction beneath the retaining ring, enabling enhanced heat dissipation and consequently reducing the maximum operating temperature. Conversely, the solid ring, in direct contact with the lens, experiences a higher temperature due to the decreased thermal conductivity caused by the presence of the holes, impeding heat transfer away from the lens.

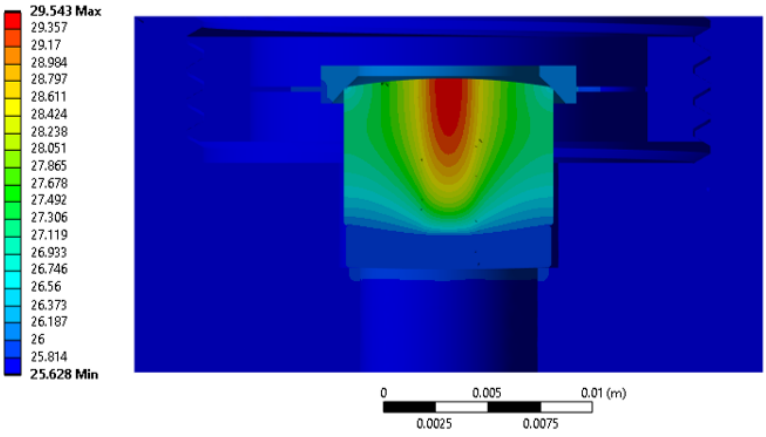

Figure 59: Operating temperature in concept 2 of the coupler mount

3.4.2 Static Structural Analysis

The discrepancy in the CTE between the coupler mount and the lenses gives rise to significant principal tensile and compressive stresses within the lenses if the temperature decreases to $-25°C$. The respective maximum values, as depicted in Figure 60, amount to 5.81 MPa for tensile stress and 5.22 MPa for compressive stress. It is noteworthy that these stress magnitudes fall within the prescribed maximum allowable limit of 7 MPa. Hence, there exists a safety factor of 1.2, which indicates a sufficient margin of safety.

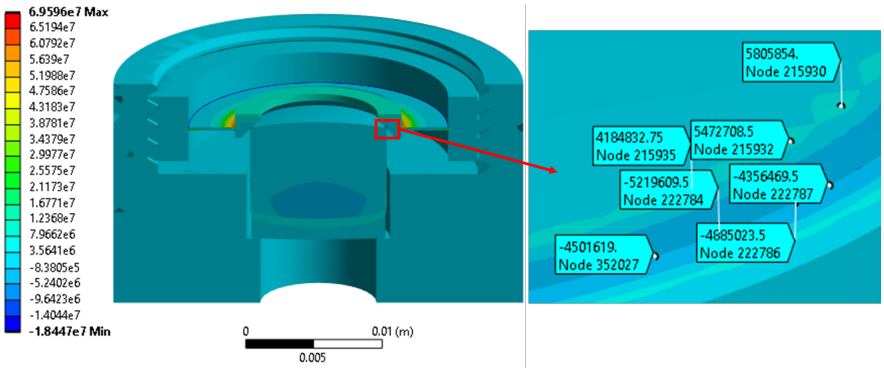

Figure 60: Principle stresses in concept 1 of the coupler mount

The magnitudes of the maximal principal tensile and compressive stresses, as shown in Figure 61, have been quantified as 3.18 MPa and 3.38 MPa, respectively. It is noteworthy that the tensile stress falls well within the prescribed maximum allowable limit of 7 MPa in tension.

Similarly, the maximal principal tensile and compressive stresses observed between the first and second lenses amount to approximately 5.86 MPa and 3.68 MPa, respectively. Furthermore, the results of preliminary thermal cycling tests involving the cemented lenses subjected to a temperature of $-25°C$ have been encouraging, revealing an absence of any fractures or cracks. These findings bolster the notion that the determined stress levels are indeed acceptable.

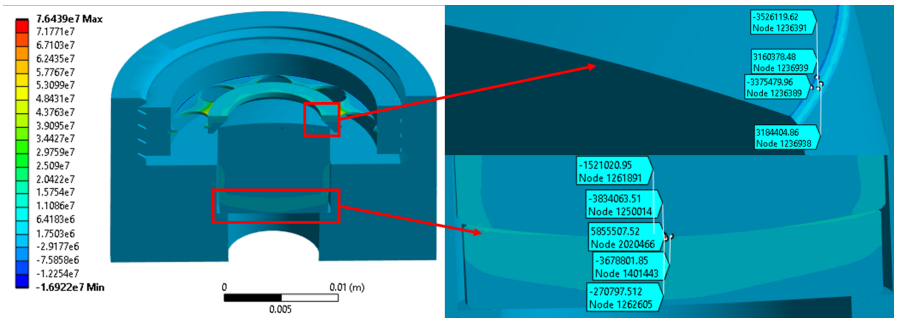

Figure 61: Principle stresses in concept 2 of the coupler mount

3.4.3 Model Analysis

The visual representation of the characteristics of the first concept's first three eigenfrequency modes can be observed in Figure 62. The first mode is characterized by a translational frequency of 48.6 kHz in the z-direction. On the other hand, modes 2 and 3 correspond to rotational motion around the x- and y-axes, with frequencies of 55.9 and 56.0 kHz, respectively. It is crucial to underscore the exceptional robustness of the underlying concept of this mount, which is further supported by the high eigenfrequency modes it exhibits.

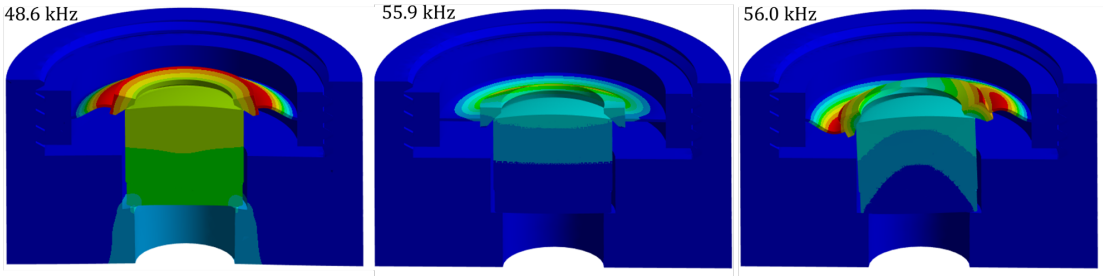

Figure 62: First three eigenfrequency modes of concept 1 of the coupler mount

The first three eigenfrequency modes of the third concept are illustrated in Figure 63. These modes offer a visual representation of their respective characteristics. It is noteworthy that these modes exhibit similar frequency orientations as those observed in concept 1. Specifically, the first three modes are associated with rotational motion around the x- and y-axes and translational motion in the z-direction, with eigenfrequency modes of 47.0 kHz, 47.0 kHz, and 49.5 kHz, respectively. However, it should be noted that this concept demonstrates significantly lower eigenfrequency in the rotational motion around the x- and y-axes.

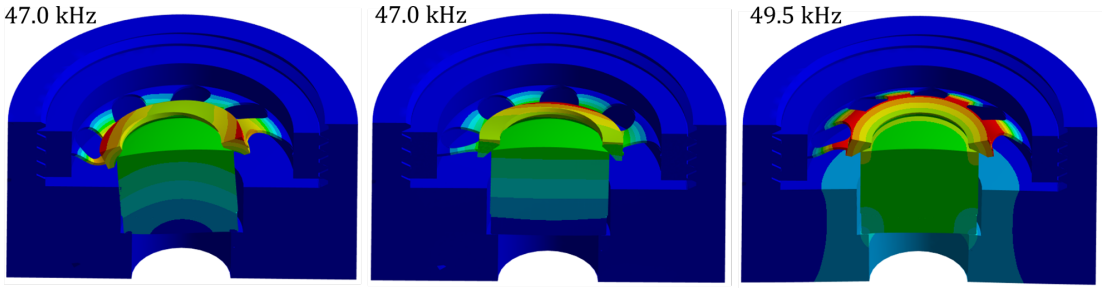

Figure 63: First three eigenfrequency modes of concept 2 of the coupler mount

4 Final Design

When selecting a final design based on factors such as maximal operating temperature, tensile and compressive stresses, eigenfrequency magnitude and profile, and manufacturability, several considerations come into play.

Firstly, the maximal operating temperature requirement should be as low as possible. This indicates good thermal dissipation away from the lens. The temperature profile is considered to be equally desired and will therefore not be included in the comparison analysis.

Next, the maximal principal tensile and compressive stresses need to be evaluated to ensure that the selected design can withstand the expected loads due to transport conditions. The tensile stresses may not exceed 7 MPa to confidently say that the lenses will not fracture or crack.

The determination of eigenfrequency magnitude and profile ensures structural stability and prevents resonance occurrences. Modal analysis was conducted to ascertain the natural frequencies and their corresponding mode shapes. It is imperative that these frequencies remain well above

the operational frequency range of 5 Hz to 2 kHz to prevent resonance, which could result in undesired vibrations or failures. The first mode's frequency profile is evaluated. If this mode corresponds to a rotation around the optical axis or translation in the z-direction, the influence on the optical performance is considered minimal and thus assigned a ranking of 3. In comparison, the translational frequencies along the x- and y-axes exhibit reduced alignment errors compared to rotational frequencies around the respective axes, resulting in rankings of 2 and 1, respectively.

The assessment of manufacturability entails a rigorous examination of the design's viability, considering the available manufacturing processes and techniques. In this context, a thorough scale ranging from 1 to 3 is employed to assign scores, which indicate the degree of ease associated with the manufacturing process as well as the number of involved manufacturing steps. A score of 1 signifies a challenging manufacturing process, while a score of 3 denotes a relatively straightforward manufacturing process.

The presented figures in this study serve to elucidate the performance of the mounts. In particular, Figure 64 and Figure 65 provide a comprehensive overview of the mount's performance, offering a visual representation of the analyzed data. Furthermore, for a more detailed examination of the results, Table 2 and Table 3 present a comprehensive listing of the numerical findings obtained from the analysis.

4.1 Final Design Collimator Mount

Among the three collimator concepts considered, Concept 3 emerged as the most promising option, demonstrating an optimal balance between Concepts 1 and 2. Concept 3 offers several advantages over the current collimator mount, including ease of manufacture, high stiffness, low operating temperatures, and reduced stress levels. Moreover, the eigenfrequency first mode of Concept 3 exhibits a noteworthy improvement when compared to the current design.

Based on these findings, it can be inferred that the implementation of Concept 3 is expected to lead to enhancement stability while relaxing manufacturing constraints, thus offering a compelling solution for addressing the challenges associated with the collimator lens mounting in the ULS.

Table 2: Numerical analysis results on the collimator mounts

Collimator Concepts	Operation temperature	Tensile stress	Compresive stress	Lowest eigenfrequency	Eigenfrequency profile	Manufacturability
Current Concept	25.21 °C	7.56 MPa	3.72 MPa	9.1 kHz	1	1
Concept 1	23.82 °C	12.50 MPa	38.77 MPa	37.5 kHz	3	3
Concept 2	24.32 °C	0.55 MPa	1.63 MPa	27.8 kHz	3	2
Concept 3	23.92 °C	5.78 MPa	8.00 MPa	32.7 kHz	3	3

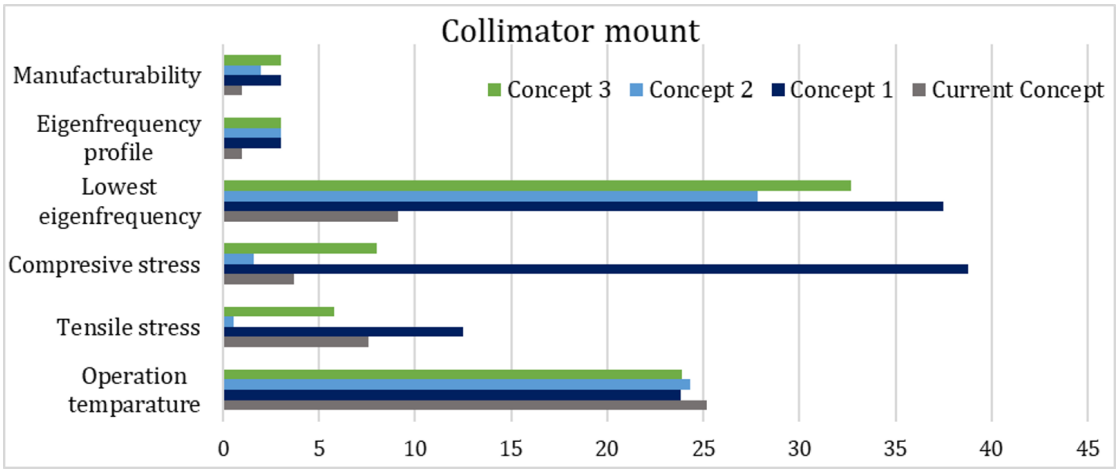

Figure 64: Compression graph of the analysis results of the collimator mounts

The optimized self-centering collimator lens mount exhibits centering error, which is influenced by various tolerances. To comprehensively assess the overall centering error of the system, we employ the Root Square Mean (RSM) analysis. The RSM method is utilized to evaluate the cumulative effect of tolerances within the mounting mechanism. It involves selecting the worst-case scenario of tolerance distribution and subsequently applying the RSM to determine the resulting centering errors. These tolerances have a deviation of $\pm 0.2\%$ for the lens radial surface, $\pm 1^{\circ}$ for the thread angle, and ± 0.2 mm for the remaining parameters. The calculated centering errors for lens 1 and lens 2 are 7.01 μm and 6.92 μm, respectively.

However, it is important to note that these results are theoretical in nature and require validation through experimental data to ascertain their accuracy. Hence, further research is essential to confirm these values and ensure the reliability of the lens mount in practical applications.

4.2 Final Design Coupler Mount

Among the two coupler mount concepts, the self-centering design has emerged as the most promising option, demonstrating numerous advantages over the current coupler mount. These advantages include ease of manufacture, high stiffness, and reduced stress levels. However, it should be noted that the self-centering design operates at higher temperatures. Furthermore, an important improvement is observed in the eigenfrequency first mode of the Concepts when compared to the current design. Although Concepts 1 and 2 exhibit similar performance, the higher stiffness and higher ease of manufacturing make concept 1 more suitable for the application at hand.

Based on these findings, it can be inferred that the implementation of Concept 1 is expected to result in enhanced overall performance compared to the current mounting mechanism. Consequently, it offers a compelling solution for addressing the challenges associated with the coupler lens mounting in the ULS.

Table 3: Numerical analysis results on the coupler mounts

Coupler Concepts	Operation temperature	Tensile stress	Compresive stress	Lowest eigenfrequency	Eigenfrequency profile	Manufactur-ability
Current Concept	27.54 °C	16.73 Mpa	3.72 MPa	27.4 kHz	2	1
Concept 1	29.91 °C	5.81 Mpa	5.22 MPa	48.6 kHz	3	3
Concept 2	29.54 °C	3.18 Mpa	3.38 MPa	47.0 kHz	2	2

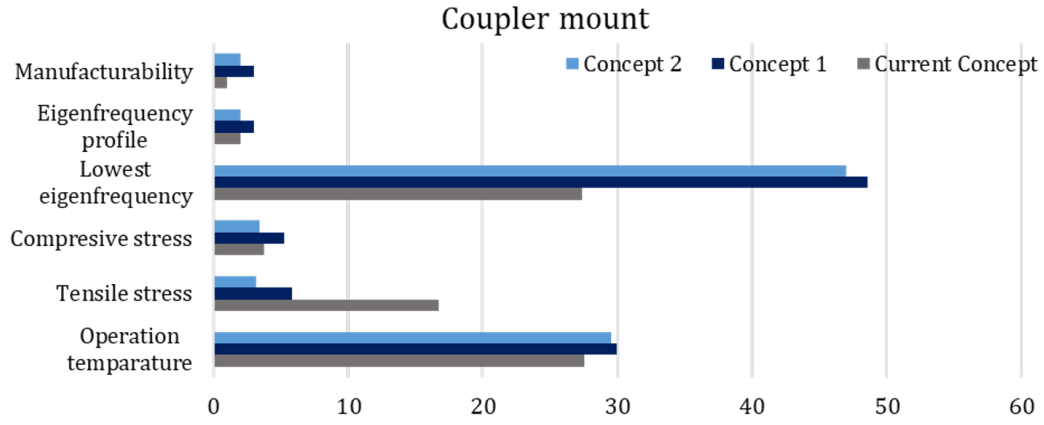

Figure 65: Compression graph of the analysis results of the coupler mounts

The optimized self-centering coupler lens mount exhibits centering error, which is influenced by various tolerances. These tolerances include a $\pm 0.2mm$ deviation for the radial contact surface, a $\pm 1^{\circ}$ variation in the thread angle, and a ± 0.2 mm fluctuation in the remaining parameters. The specific centering error value, determined to be $6.27\mu m$, is calculated based on these tolerance limits. It is important to emphasize that further research is required to corroborate these numerical values with experimental data. Only through such experimental validation can we validate the accuracy and reliability of our calculations in real-world scenarios.

5 Discussion

This study explores an optimized self-centering lens mounting technique for collimator and coupler lenses in ULS. The current flexure mounting design is associated with adhesion-related risks and stringent manufacturing tolerances, necessitating the development of a self-centering approach that leverages geometric relationships to minimize positioning errors. Through detailed calculations, it is demonstrated that the proposed optimization of the self-centering technique enables high position accuracy within a few micrometers while relaxing manufacturing tolerances. Additionally, simulations reveal that the proposed symmetrical design with strategically located flexibility has improved dynamical stability while maintaining acceptable stress levels and eliminating the need for adhesives. As a result, the mounts will exhibit improved reliability and increased lifetime, while also alleviating manufacturing and assembly challenges.

However, it is essential to acknowledge several limitations inherent in this study. Firstly, the generalizability of the results is limited by the specific geometry of the lenses under investigation. Lenses with high convexity generally exhibit improved centering error performance compared to nearly flat lenses. Consequently, the analysis is focused on the coupler and collimator lenses, warranting further investigation into other lens geometries and scales, such as biconcave lenses or lenses with a diameter of 100+ mm, to comprehensively evaluate the applicability of the optimized self-centering technique.

Furthermore, a key limitation stems from the study's reliance on theoretical data, which may deviate slightly from practical cases. The unavailability of experimental data is attributed to challenges associated with accurately measuring centering error with a precision of $\pm 0.1 \mu m$. While the Trioptics OptoCentric, capable of such measurements, is housed in the ASML Wilton office, the process of finding a suitable supplier, manufacturing lead time, and scheduling and programming the equipment resulted in substantial delays far beyond the time frame of this project.

In conclusion, this study establishes the effectiveness of an optimized self-centering lens mounting technique in enhancing positioning accuracy and stability within ULS systems. Despite the acknowledged limitations, the findings presented herein provide a valuable foundation for further research and development in the field of lens mounting methodologies and their applications in advanced optical systems.

6 Conclusion

Self-centering advancements in lens mounting for optomechanics offer significant potential for improving the precision and performance of optical systems without the use of adhesives. This study focused on investigating the implications of self-centering for the coupler and collimator mounts, using a practical case study approach. Through extensive analysis and optimization of self-centering parameters, valuable insights were obtained.

The optimization process revealed that increasing the parameters d_{ring} and y, while setting h to $-\alpha/2$, resulted in significantly reduced centering errors. For the collimator lens 2, with a typical self-centered barrel configuration, the calculated centering error was found to be $33.03 \mu m$. Seeking to improve the design and enhance its centering accuracy, the parameters d_{ring} and y were increased, while h was set to $-\alpha/2$ in design B. Consequently, the thread angle was calculated to be 1.37 radians or 78.57 degrees, and the corresponding thread clearance was reduced to 0.306 mm. This optimization led to a substantial reduction of 78% in the centering error, which now measures $7.12 \mu m$. Moreover, a systematic analysis of tolerances emphasized that further

centering improvements may be achieved by stricter tolerances on parameters with a significant influence on centering errors, such as φ_{thread} and R, while allowing more relaxed tolerances on other parameters.

The analysis of sliding and tipping behavior indicated that the self-centering method with the lens edge as the interface could be effectively applied to the coupler lenses. However, the friction coefficient played a crucial role in determining whether sliding or tipping occurred, necessitating careful consideration of the clamping force and frictional characteristics.

Thermal effects were identified as critical considerations in designing the mounts to maintain stability and prevent image quality degradation due to birefringence. Strategically positioned flexibility and a symmetrical design were recommended to mitigate the impact of temperature fluctuations.

Finally, the study proposed different mounting concepts for both the coupler and collimator lenses, taking into account various factors such as stiffness, flexibility, thermal stability, and manufacturing challenges. The selected concept must strike a balance between mounting rigidity and minimizing tensile stresses induced by thermal effects. The selection process involved evaluating various factors, including maximal operating temperature, tensile and compressive stresses, eigenfrequency magnitude and profile, and manufacturability.

Regarding maximal operating temperature, a low-temperature requirement was deemed essential to ensure efficient thermal dissipation away from the lens. The evaluation of maximal principal tensile and compressive stresses revealed in the current designs and collimator concept 1 tensile stress surpassing the required 7 MPa to prevent fractures or cracks in the lenses. Eigenfrequency magnitude and profile analysis were conducted to ensure structural stability and avoid resonance occurrences, with frequencies required to remain well above the operational frequency range of 5 Hz to 2 kHz.

Among the collimator concepts, Concept 3 emerged as the most promising option due to its optimal balance between Concepts 1 and 2, offering advantages such as ease of manufacture, high stiffness, low operating temperatures, and reduced stress levels. For the coupler mounts, the self-centering design of Concept 1 was found to be superior, boasting higher stiffness and ease of manufacturing compared to Concept 2.

The resulting optimized self-centering lens mount concepts exhibited centering errors, which were affected by various tolerances. These tolerances included a deviation of $\pm 0.2\%$ for the lens radial surface, $\pm 1^{\circ}$ for the thread angle, and ± 0.2 mm for the remaining parameters. The calculated centering errors for the coupler lens and collimator lenses 1 and 2 were determined to be $6.27 \mu m$, $7.01\ \mu m$, and $6.92\ \mu m$, respectively.

Overall, this research contributes to the understanding and advancement of self-centering techniques in optomechanics. It provides valuable guidelines and recommendations for designing self-centering lens mounts with enhanced optical performance and reliability, facilitating advancements in optical systems and applications.

References

[1] S. Liu, Y. Wang, *et al.*, "Anti-resonant reflecting guidance in alcohol-filled hollow core photonic crystal fiber for sensing applications," *Opt. Express*, vol. 21, no. 25, pp. 31 690–31 697, Dec 2013. [Online]. Available: https://opg.optica.org/oe/abstract.cfm?URI=oe-21-25-31690

[2] C.-H. Lai, B. You, *et al.*, "Modal characteristics of antiresonant reflecting pipe waveguides for terahertz waveguiding," *Opt. Express*, vol. 18, no. 1, pp. 309–322, Jan 2010. [Online]. Available: https://opg.optica.org/oe/abstract.cfm?URI=oe-18-1-309

[3] G. Shou-Fei, W. Ying-Ying, *et al.*, "From raman frequency combs to supercontinuum generation in nitrogen-filled hollow-core anti-resonant fiber," *Laser & Photonics Reviews*, vol. 16, no. 4, p. 2100426, 2022. [Online]. Available: https://onlinelibrary.wiley.com/doi/abs/10.1002/lpor.202100426

[4] P. St. J. Russell, P. Hölzer, *et al.*, "Hollow-core photonic crystal fibres for gas-based nonlinear optics," *Nature Photonics*, vol. 8, no. 4, pp. 278–286, 2014. [Online]. Available: https://doi.org/10.1038/nphoton.2013.312

[5] M. F. Saleh, A. Armaroli, *et al.*, "Raman-induced temporal condensed matter physics in gas-filled photonic crystal fibers," *Opt. Express*, vol. 23, no. 9, pp. 11 879–11 886, May 2015. [Online]. Available: https://opg.optica.org/oe/abstract.cfm?URI=oe-23-9-11879

[6] L. Chen, M. Liao, *et al.*, "Flat supercontinuum generation by spectral shaping with anti-resonant hollow-core fiber," in *Eighth Symposium on Novel Photoelectronic Detection Technology and Applications*, J. Su, L. Chen, *et al.*, Eds., vol. 12169, International Society for Optics and Photonics. SPIE, 2022, p. 121698R. [Online]. Available: https://doi.org/10.1117/12.2625182

[7] Adamu I. Abubakar, Md. Habib Selim, *et al.*, "Deep-uv to mid-ir supercontinuum generation driven by mid-ir ultrashort pulses in a gas-filled hollow-core fiber," vol. 9. Scientific Reports, 2019, pp. 2045–2322. [Online]. Available: https://doi.org/10.1038/s41598-019-39302-2

[8] J. C. Travers, W. Chang, *et al.*, "Ultrafast nonlinear optics in gas-filled hollow-core photonic crystal fibers," *J. Opt. Soc. Am. B*, vol. 28, no. 12, pp. A11–A26, Dec 2011. [Online]. Available: https://opg.optica.org/josab/abstract.cfm?URI=josab-28-12-A11

[9] Y. Wan, M. I. Hasan, *et al.*, "Impact of mode-area dispersion on nonlinear pulse propagation in gas-filled anti-resonant hollow-core fiber," *Photonics*, vol. 9, no. 1, 2022. [Online]. Available: https://www.mdpi.com/2304-6732/9/1/25

[10] J. Teipel, K. Franke, *et al.*, "Characteristics of supercontinuum generationin tapered fibers using femtosecond laser pulses," vol. 77. Applied Physics B, 2003, pp. 245–251. [Online]. Available: https://doi.org/10.1007/s00340-003-1218-3

[11] A. Abdolvand, S. Bauerschmidt, *et al.*, "Hollow core fiber light source and a method for manufacturing a hollow core fiber," May 2022, date of filing: 13.11.2020, Application number: 20207371.4. [Online]. Available: https://data.epo.org/publication-server/document?iDocId=6827678&iFormat=0

[12] C. van de Vin, P. Teunissen, *et al.*, "A universal light source," in *Technology Matters*, S. C. (Pyramidion), Ed., vol. Issue 02, ASML. ASML Technical Publication Board, 2022, pp. 5–7. [Online]. Available: https:

//my.asml.com/sectors/bf/de/Documents/Technology_magazine/ASML_technology%20matters_digital%20version.HYPERLINKS.pdf#search=technology%20matters

[13] B. McMaster, "Opto-mechanical review of a light weight compact visible zoom camera," in *Airborne Intelligence, Surveillance, Reconnaissance (ISR) Systems and Applications VII*, D. J. Henry, Ed., vol. 7668, International Society for Optics and Photonics. SPIE, 2010, p. 76680E. [Online]. Available: https://doi.org/10.1117/12.858795

[14] D. V. Yoder Jr, Paul R, *Opto-mechanical systems design*. CRC press, 2015. [Online]. Available: https://doi.org/10.1201/9781315217635

[15] H. Gilbergs, N. Wengert, *et al.*, "Reconstruction of dynamical perturbations in optical systems by opto-mechanical simulation methods," in *Optical Microlithography XXV*, W. Conley, Ed., vol. 8326, International Society for Optics and Photonics. SPIE, 2012, p. 83262N. [Online]. Available: https://doi.org/10.1117/12.916615

[16] X. Liu, J. Guo, *et al.*, "Research on the influence of alignment error on coupling efficiency and beam quality for gaussian beam to multimode fiber," *Results in Physics*, vol. 12, pp. 1044–1049, 2019. [Online]. Available: https://www.sciencedirect.com/science/article/pii/S2211379718316851

[17] J. Niu and J. Xu, "Coupling efficiency of laser beam to multimode fiber," *Optics Communications*, vol. 274, no. 2, pp. 315–319, 2007. [Online]. Available: https://www.sciencedirect.com/science/article/pii/S0030401807002003

[18] A. Srivastava and D. Goswami, "Control of supercontinuum generation with polarization of incident laser pulses," *Applied Physics B*, vol. 77, no. 2-3, pp. 325–328, 2003.

[19] A. Proulx, J.-M. Ménard, *et al.*, "Intensity and polarization dependences of the supercontinuum generation in birefringent and highly nonlinear microstructured fibers," *Opt. Express*, vol. 11, no. 25, pp. 3338–3345, Dec 2003. [Online]. Available: https://opg.optica.org/oe/abstract.cfm?URI=oe-11-25-3338

[20] L. Hahn, J. Störkle, *et al.*, "Consideration of polarization during the ray tracing for mechanically stressed lenses in dynamical-optical systems," *Optik*, vol. 193, p. 162923, 2019. [Online]. Available: https://www.sciencedirect.com/science/article/pii/S0030402619308009

[21] P. Giesen and E. Folgering, "Design guidelines for thermal stability in optomechanical instruments," in *Optomechanics 2003*, A. E. Hatheway, Ed., vol. 5176, International Society for Optics and Photonics. SPIE, 2003, pp. 126 – 134. [Online]. Available: https://doi.org/10.1117/12.510285

[22] T. H. Jamieson, "Thermal Effects In Optical Systems," *Optical Engineering*, vol. 20, no. 2, p. 202156, 1981. [Online]. Available: https://doi.org/10.1117/12.7972683

[23] M. Lipp, E. Langenbach, *et al.*, "Passive thermal stabilization," in *International Optical Design Conference 2014*, M. Figueiro, S. Lerner, *et al.*, Eds., vol. 9293, International Society for Optics and Photonics. SPIE, 2014, p. 929323. [Online]. Available: https://doi.org/10.1117/12.2074265

[24] T. P. O'Brien and B. Atwood, "Lens mounting system for cryogenic applications," in *Instrument Design and Performance for Optical/Infrared Ground-based Telescopes*, M. Iye and A. F. M. Moorwood, Eds., vol. 4841, International Society for Optics and Photonics. SPIE, 2003, pp. 398 – 402. [Online]. Available: https://doi.org/10.1117/12.459960

[25] S. Barrera, A. Villegas, *et al.*, "EMIR optomechanics," in *Astronomical Structures and Mechanisms Technology*, J. Antebi and D. Lemke, Eds., vol. 5495, International Society for Optics and Photonics. SPIE, 2004, pp. 611 – 621. [Online]. Available: https://doi.org/10.1117/12.550463

[26] D. Vukobratovich and P. Yoder, *Fundamentals of Optomechanics*, ser. Optical Sciences and Applications of Light. CRC Press, 2018. [Online]. Available: https://books.google.nl/books?id=bmpQDwAAQBAJ

[27] S. A. Smee, "A precision lens mount for large temperature excursions," in *Modern Technologies in Space- and Ground-based Telescopes and Instrumentation*, E. Atad-Ettedgui and D. Lemke, Eds., vol. 7739, International Society for Optics and Photonics. SPIE, 2010, p. 77393O. [Online]. Available: https://doi.org/10.1117/12.858038

[28] T. R. Froud, I. A. J. Tosh, *et al.*, "Cryogenic mounts for large fused silica lenses," in *Optomechanical Technologies for Astronomy*, E. Atad-Ettedgui, J. Antebi, *et al.*, Eds., vol. 6273, International Society for Optics and Photonics. SPIE, 2006, p. 62732I. [Online]. Available: https://doi.org/10.1117/12.670198

[29] B. M. McMaster, R. D. Grejda, *et al.*, "Advancements in adhesive mounting of optics," in *Optomechanical Engineering 2017*, A. E. Hatheway and D. M. Stubbs, Eds., vol. 10371, International Society for Optics and Photonics. SPIE, 2017, p. 1037103. [Online]. Available: https://doi.org/10.1117/12.2275977

[30] I. M. Plitz, O. S. Gebizlioglu, *et al.*, "Reliability characterization of UV-curable adhesives used in optical devices," in *Fiber Optic Materials and Components*, H. H. Yuce, D. K. Paul, *et al.*, Eds., vol. 2290, International Society for Optics and Photonics. SPIE, 1994, pp. 150 – 159. [Online]. Available: https://doi.org/10.1117/12.187412

[31] J. G. Daly and M. D. Hawk, "Adhesive bonds for optics: analysis and trade-offs," in *Optomechanical Engineering 2017*, A. E. Hatheway and D. M. Stubbs, Eds., vol. 10371, International Society for Optics and Photonics. SPIE, 2017, p. 1037102. [Online]. Available: https://doi.org/10.1117/12.2275713

[32] C. Cai, D. C. Miller, *et al.*, "Degradation of thermally-cured silicone encapsulant under terrestrial uv," *Solar Energy Materials and Solar Cells*, vol. 157, pp. 346–353, 2016. [Online]. Available: https://www.sciencedirect.com/science/article/pii/S0927024816301726

[33] F. Maamar and A. Boudjemai, "Optomechanical optimal design configuration and analysis of glue pad bonds in lens mounting for space application," *Advances in Space Research*, vol. 65, no. 10, pp. 2263–2275, 2020. [Online]. Available: https://www.sciencedirect.com/science/article/pii/S0273117720300430

[34] J. G. Daly and D. J. Daly, "Structural adhesives for bonding optics to metals: a study of optomechanical stability," in *Optomechanical Design and Engineering 2001*, A. E. Hatheway, Ed., vol. 4444, International Society for Optics and Photonics. SPIE, 2001, pp. 177 – 184. [Online]. Available: https://doi.org/10.1117/12.447299

[35] W. Cai, B. Cuerden, *et al.*, "Strength of glass from Hertzian line contact," in *Optomechanics 2011: Innovations and Solutions*, A. E. Hatheway, Ed., vol. 8125, International Society for Optics and Photonics. SPIE, 2011, p. 81250E. [Online]. Available: https://doi.org/10.1117/12.893583

[36] C. Ottens and R. Beerens, "Gid design guidelines for opto-mechanical assemblies." ASML, 2014, pp. 53–56, 38175-12-GID-001.

[37] K. A. Sawyer, "Contact stresses and their optical effects in biconvex optical elements," in *Optomechanical and Precision Instrument Design*, A. E. Hatheway, Ed., vol. 2542, International Society for Optics and Photonics. SPIE, 1995, pp. 58 – 69. [Online]. Available: https://doi.org/10.1117/12.218681

[38] D. Vukobratovich and P. Yoder, *Fundamentals of Optomechanics*, ser. Optical Sciences and Applications of Light. CRC Press, 2018. [Online]. Available: https://books.google.nl/books?id=bmpQDwAAQBAJ

[39] J. B. Katie Schwertz, *Field Guide to Optomechanical Design and Analysis*, ser. Clamped Flange Mount. Spie, 2012. [Online]. Available: https://doi.org/10.1117/3.934930.ch56

[40] D. Vukobratovich and R. M. Richard, "Flexure Mounts For High-Resolution Optical Elements," in *Optomechanical and Electro-Optical Design of Industrial Systems*, R. J. Bieringer and K. G. Harding, Eds., vol. 0959, International Society for Optics and Photonics. SPIE, 1988, pp. 18 – 36. [Online]. Available: https://doi.org/10.1117/12.947774

[41] P. R. Y. Jr., *Mounting Optics in Optical Instruments, 2nd Edition*, ser. Mounting Individual Lenses. SPIE, 2008. [Online]. Available: https://doi.org/10.1117/3.785236.ch2

[42] P. Ribes, C. Koechlin, *et al.*, "High-precision opto-mechanical lens system for space applications assembled by innovative local soldering technique," in *Integrated Optics: Devices, Materials, and Technologies XX*, J.-E. Broquin and G. N. Conti, Eds., vol. 9750, International Society for Optics and Photonics. SPIE, 2016, p. 97501K. [Online]. Available: https://doi.org/10.1117/12.2208123

[43] Y. Gao and B. Zhang, "Design and analysis for the flexible support structure of high precision lens assembly," *Optik*, vol. 175, pp. 228–236, 2018. [Online]. Available: https://www.sciencedirect.com/science/article/pii/S0030402618313342

[44] R. H. Barkhouser, S. A. Smee, *et al.*, "Optical and optomechanical design of the WIYN High Resolution Infrared Camera," in *Ground-based Instrumentation for Astronomy*, A. F. M. Moorwood and M. Iye, Eds., vol. 5492, International Society for Optics and Photonics. SPIE, 2004, pp. 921 – 931. [Online]. Available: https://doi.org/10.1117/12.578365

[45] H. Kihm, H.-S. Yang, *et al.*, "Athermal lens mount with ring flexures," *Journal of the Korean Physical Society*, vol. 59, no. 6, pp. 3356–3362, 2011.

[46] F. Lamontagne, N. Desnoyers, *et al.*, "Lens auto-centering," in *Optical Systems Design 2015: Optical Design and Engineering VI*, L. Mazuray, R. Wartmann, *et al.*, Eds., vol. 9626, International Society for Optics and Photonics. SPIE, 2015, p. 962619. [Online]. Available: https://doi.org/10.1117/12.2196756

[47] D. Vukobratovich and P. Yoder, *Fundamentals of Optomechanics*. CRC Press, 2018. [Online]. Available: https://books.google.nl/books?id=bmpQDwAAQBAJ

[48] P. Yoder and D. Vukobratovich, *Opto-Mechanical Systems Design, Design and Analysis of Opto-Mechanical Assemblies*, 4th ed. CRC Press, 2015, vol. 1. [Online]. Available: https://books.google.nl/books?id=bmpQDwAAQBAJ

[49] F. Lamontagne, N. Desnoyers, *et al.*, "Disruptive advancement in precision lens mounting," in *Optical System Alignment, Tolerancing, and Verification IX*, J. Sasián and R. N.

Youngworth, Eds., vol. 9582, International Society for Optics and Photonics. SPIE, 2015, p. 95820D. [Online]. Available: https://doi.org/10.1117/12.2196441

[50] ——, "High precision optomechanical assembly using threads as mechanical reference," vol. 9951, p. 995107, 2016. [Online]. Available: https://doi.org/10.1117/12.2237654

[51] F. Lamontagne, M. Savard, *et al.*, "Lens centering using edge contact mounting," in *Optical Modeling and System Alignment*, M. A. Kahan, J. Sasián, *et al.*, Eds., vol. 11103, International Society for Optics and Photonics. SPIE, 2019, p. 1110304. [Online]. Available: https://doi.org/10.1117/12.2528728

[52] ——, "High accuracy lens centering using edge contact mounting," *Optical Engineering*, vol. 60, no. 5, p. 051212, 2021. [Online]. Available: https://doi.org/10.1117/1.OE.60.5.051212

[53] "ISO general purpose screw threads — Basic profile - Part 1: Metric screw threads," in *ISO 68-1:1998*, the International Organization for Standardization. ISO, 1998, p. 3. [Online]. Available: https://www.iso.org/ics/21.040.10/x/

[54] F. Lamontagne and N. Desnoyers, "Auto-centering of an optical element within a barrel," May 2015, date of filing: 11.07.2014, Application number: PCT/CA2014/050660. [Online]. Available: https://patentscope.wipo.int/search/en/detail.jsf?docId=WO2015066801

[55] *S-NBM51, Optical Glass, Data sheet*, OHARA GmbH, Hofheim Germany, 12 2019. [Online]. Available: https://www.ohara-gmbh.com/fileadmin/user_upload/export-data/pdf/product_datasheets/S-NBM51_English_.pdf

[56] *Optical Glass, Data sheet*, SCHOTT North America, Inc, Advanced Optics, 7 2015, N-FK58, page: 8, N-LAK22, page: 54, N-SF6HT, page: 97. [Online]. Available: https://wp.optics.arizona.edu/jgreivenkamp/wp-content/uploads/sites/11/2016/01/schott-optical-glass-collection-datasheets-july-2015-us.pdf

[57] C.-Y. Huang, C.-F. Ho, *et al.*, "Alignment turning system for precision lens cells," *The International Journal of Advanced Manufacturing Technology*, vol. 100, no. 5, pp. 1383–1392, 2019. [Online]. Available: https://link.springer.com/article/10.1007/s00170-018-2699-x

[58] K. Eijsvogels, "Generic Standard of ASML, Manufacturing general geometrical specifications." ASML, 2008, pp. 1–34, gSA 02 0102.

[59] H. Sun, *Basic Optical Engineering for Engineers and Scientists*, ser. Lens Fabrication, Tolerances, Procurement, Inspection, and Mounting. SPIE, 2019. [Online]. Available: https://doi.org/10.1117/3.2504404.ch14